scientific reports

Check for updates

OPEN

Molecular simulations unravel the molecular principles that mediate selective permeability of carboxysome shell protein

Matthew Faulkner[1,5], István Szabó[2,5], Samantha L. Weetman[1,3,5], Francois Sicard[2], Roland G. Huber[3], Peter J. Bond[3], Edina Rosta[2]✉ & Lu-Ning Liu[1,4]✉

Bacterial microcompartments (BMCs) are nanoscale proteinaceous organelles that encapsulate enzymes from the cytoplasm using an icosahedral protein shell that resembles viral capsids. Of particular interest are the carboxysomes (CBs), which sequester the CO_2-fixing enzymes ribulose-1,5-bisphosphate carboxylase/oxygenase (Rubisco) to enhance carbon assimilation. The carboxysome shell serves as a semi-permeable barrier for passage of metabolites in and out of the carboxysome to enhance CO_2 fixation. How the protein shell directs influx and efflux of molecules in an effective manner has remained elusive. Here we use molecular dynamics and umbrella sampling calculations to determine the free-energy profiles of the metabolic substrates, bicarbonate, CO_2 and ribulose bisphosphate and the product 3-phosphoglycerate associated with their transition through the major carboxysome shell protein CcmK2. We elucidate the electrostatic charge-based permeability and key amino acid residues of CcmK2 functioning in mediating molecular transit through the central pore. Conformational changes of the loops forming the central pore may also be required for transit of specific metabolites. The importance of these in-silico findings is validated experimentally by site-directed mutagenesis of the key CcmK2 residue Serine 39. This study provides insight into the mechanism that mediates molecular transport through the shells of carboxysomes, applicable to other BMCs. It also offers a predictive approach to investigate and manipulate the shell permeability, with the intent of engineering BMC-based metabolic modules for new functions in synthetic biology.

Bacterial microcompartments (BMCs) are proteinaceous organelles that sequester key metabolic pathways in the cytoplasm to enhance metabolic performance[1]. These metabolic modules are ubiquitous in many bacterial phyla and play vital roles in CO_2 fixation, pathogenesis, and microbial ecology[2–4]. BMCs are composed of catalytic enzymes encapsulated by a single-layer protein shell that structurally resembles virus capsids. The shell is self-assembled by hundreds of proteins in the forms of hexamers (BMC-H), pentamers (BMC-P) and trimers (BMC-T). BMC-H and BMC-T proteins are predominant in the shell facets, whereas BMC-P proteins occupy the vertices of the polyhedral shell[5].

The most well-characterized BMC is the carboxysome, which acts as the key CO_2-fixing machinery in all cyanobacteria and many chemoautotrophs[6–8]. The primary carboxylating enzymes, ribulose-1,5-bisphosphate carboxylase/oxygenase (Rubisco), are encased in the carboxysome[9]. Based on their protein composition and phylogeny of Rubisco enzymes, carboxysomes can be categorized into two types, α-carboxysomes and β-carboxysomes[10]. The β-carboxysome from freshwater cyanobacteria exhibits an icosahedral geometry with a diameter of ~ 150 nm (Fig. 1A)[11,12].

Rubisco catalyzes the reaction between ribulose-1,5-bisphosphate (RuBP) and CO_2 to generate two molecules of 3-phosphoglycerate (3-PGA). Meanwhile, Rubisco can also carry out oxygenation by accepting O_2 as a substrate instead of CO_2 through a competing, unproductive reaction called photorespiration. Its restricted

[1]Institute of Integrative Biology, University of Liverpool, Crown Street, Liverpool L69 7ZB, UK. [2]Department of Chemistry, King's College London, London SE1 1DB, UK. [3]Agency for Science, Technology and Research (A*STAR), Bioinformatics Institute, Matrix, Singapore 138671, Singapore. [4]College of Marine Life Sciences, and Frontiers Science Center for Deep Ocean Multispheres and Earth System, Ocean University of China, Qingdao 266003, China. [5]These authors contributed equally: Matthew Faulkner, István Szabó and Samantha L. Weetman. ✉email: edina.rosta@kcl.ac.uk; luning.liu@liverpool.ac.uk

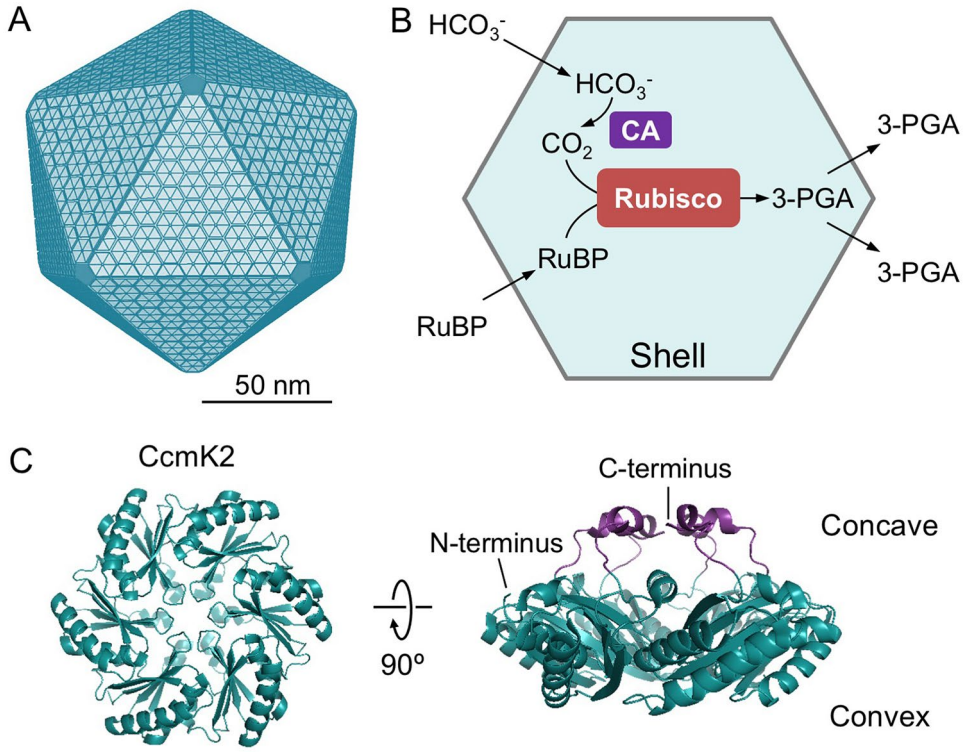

Figure 1. Carboxysome structure, metabolism and building components. (**A**) A model of the proposed polyhedral architecture of the carboxysome. The β-carboxysome from Syn7942 is ~ 150 nm in diameter, comprising an icosahedral shell formed by hexameric and pentametric proteins. (**B**) The metabolic pathways of carbon fixation in the carboxysome. The carboxysome shell serves as a physical barrier for controlling the flux of specific metabolites in and out of the carboxysome. The shell permits passage of cytosolic bicarbonate (HCO_3^-) and ribulose-1,5-bisphosphate (RuBP) into the carboxysome. Then carbonic anhydrase (CA) in the carboxysome lumen dehydrates HCO_3^- to CO_2 and provides high levels of CO_2 close to Rubisco. Rubisco catalyzes the carboxylation of RuBP by adding CO_2 to generate 3-phosphoglycerate (3-PGA), which is transported across the shell and is metabolized via the Calvin–Benson–Bassham cycle. **C**, Structural representation of the major carboxysome shell building component, CcmK2 (PDB: 2A1B). The CcmK2 complex presents a sixfold symmetry, involving a central pore that mediates metabolite flow. CcmK2 has concave and convex faces; the C-terminal tails of CcmK2, highlighted in purple, are located at the concave side.

capability in discriminating between CO_2 and O_2 causes the catalytical inefficiency of Rubisco[13]. The carboxysome provides a microenvironment that can sequester and concentrate Rubisco enzymes from the cytoplasm (Fig. 1B); carbonic anhydrase (CA) is co-encapsulated with Rubisco within the carboxysome lumen and dehydrates HCO_3^- to CO_2 and thereby, supplies a high concentration of CO_2 in the vicinity of Rubisco. The shell of the carboxysome was also speculated to act as a diffusion barrier to HCO_3^-/CO_2 efflux and O_2 influx, thereby promoting Rubisco carboxylation[14]. The shell should also permit transit of the natural substrate RuBP and product 3-PGA. Overall, the highly-defined structure and protein organization of carboxysomes enhances the efficiency of CO_2 fixation and reduces the wasteful side reaction of photorespiration, allowing cyanobacteria to contribute up to 25% of global carbon fixation on Earth[15]. As such, there is a growing interest in repurposing carboxysomes in heterologous systems, such as *Escherichia coli* (*E. coli*) and crop plants, to profoundly boost photosynthetic carbon fixation and productivity[16–20].

All shell proteins bear a central pore surrounded by the loops of BMC-H, BMC-P and BMC-T polypeptides. These pores are presumed to provide portals for metabolite transport in and out of the carboxysome, given that shell proteins are closely packed in flat facets on the basis of observations from crystallography[21,22], electron microscopy[11,23,24] and atomic force microscopy[11,25,26]. To date, how the transition of substrates through the carboxysome shell is mediated remains enigmatic. Here, we use molecular dynamics (MD) via umbrella sampling (US) free energy calculations to explore the selective permeability of the major shell protein CcmK2 (BMC-H) in β-carboxysomes to specific substrates and products related to the reaction catalyzed by Rubisco. This study provides computational evidence for elucidating the mechanisms that mediate metabolite traffic through the carboxysome shell.

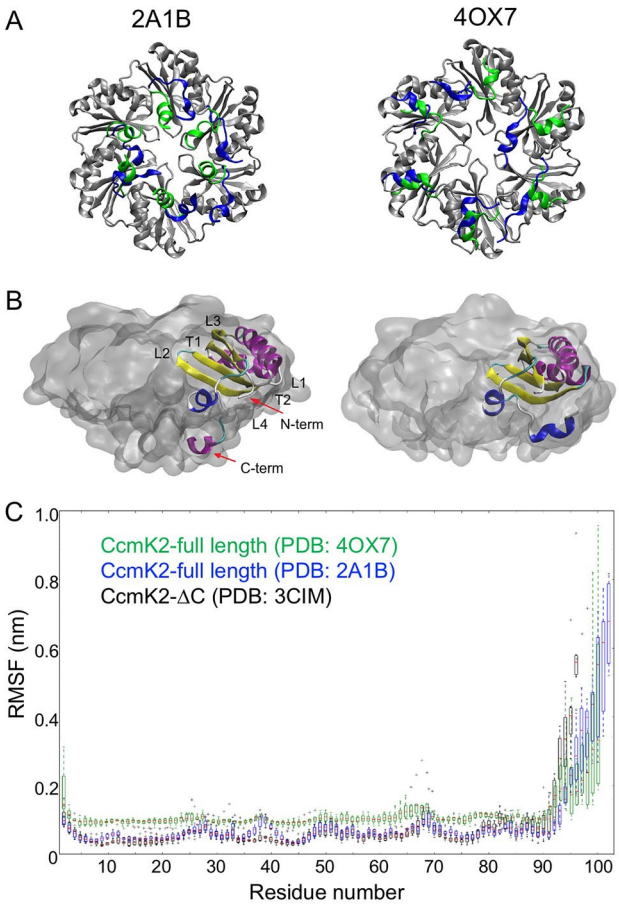

Figure 2. Structural flexibility of the C-terminal tails of CcmK2. (**A**) C-terminal orientation of CcmK2-full. The initial orientation of the C-termini is shown in green and the final state of the C-termini after 200 ns of simulation time is shown in blue. (**B**) Visualization of an individual chain (cartoon representation) in the hexamer (quick-surf representation) with the termini, loop and turn regions labeled. (**C**) RMSF profile of the truncated CcmK2 (PDB: 3CIM) and full-length CcmK2 (PDB: 2A1B and 4OX7) over the last 150 ns of the simulation period, indicating a flexible C-terminus of CcmK2.

Results

Structural flexibility of CcmK2. CcmK2 in β-carboxysomes from *Synechocystis* sp. PCC 6803 (Syn6803) was the first BMC protein that has been structurally determined[22]. The protein subunits of CcmK2 are arranged in hexameric units with a six-fold symmetry (Fig. 1C). The central pore is ~7 Å in diameter, surrounded by six copies of the backbone amide nitrogen atom of Serine 39 (Ser39). The predominant protein surface of CcmK2 is negatively charged, whereas the central pore of CcmK2 has a strong positive electrostatic potential, ascribed to the positively charged residues Arginine 11 (Arg11) and Lysine 36 (Lys36) that are 10 Å away from the narrowest point of the pore in each subunit and solvent exposed to the lumen and cytoplasm, respectively[22] (Supplementary Figures 1,2).

The CcmK2 C-terminal tail contains a 5-residue helix on the concave side and has been deduced to play roles in BMC domain assembly and protein–protein interaction[22] (Fig. 2A, B). We performed MD simulations of the full-length CcmK2 from Syn6803 (CcmK2-full, PDB: 2A1B)[22], the C-terminal truncated CcmK2 from Syn6803 (CcmK2-ΔC, PDB: 3CIM)[27], and the full-length CcmK2 from *Synechococcus elongatus* PCC 7942 (Syn7942) (PDB: 4OX7) in explicit water for 200 ns. The results revealed that the C-terminal tails of CcmK2 exhibited structural flexibility during simulations (Fig. 2C). These C-terminal residues have a lower resolution and display a higher degree of flexibility than the core residues in the crystal structures, resulting in the disorder of crystal forms[27,28]. A similar fashion of protein contacts has been illustrated in virus capsid assembly: interactions through flexible termini act as conformational switches that mediate virus capsid formation[29,30].

We conducted root mean square fluctuation (RMSF) analysis to measure the per residue fluctuation around their average positions. High values of RMSFs are seen at the C-termini (Fig. 2C), as a consequence of the high C-terminal flexibility during the course of simulations. Other regions of increased RMSF peaks correspond to regions of high flexibility such as loops and turns in CcmK2. By contrast, no significant difference in the RMSF profiles of the core regions of CcmK2 was recorded, indicative of the stable conformation of the core. To diminish the system complexity, we chose the experimentally obtained CcmK2-ΔC structure (PDB: 3CIM)[27], with a high resolution of 1.3 Å, in the following simulations to explore the molecular transport through the central

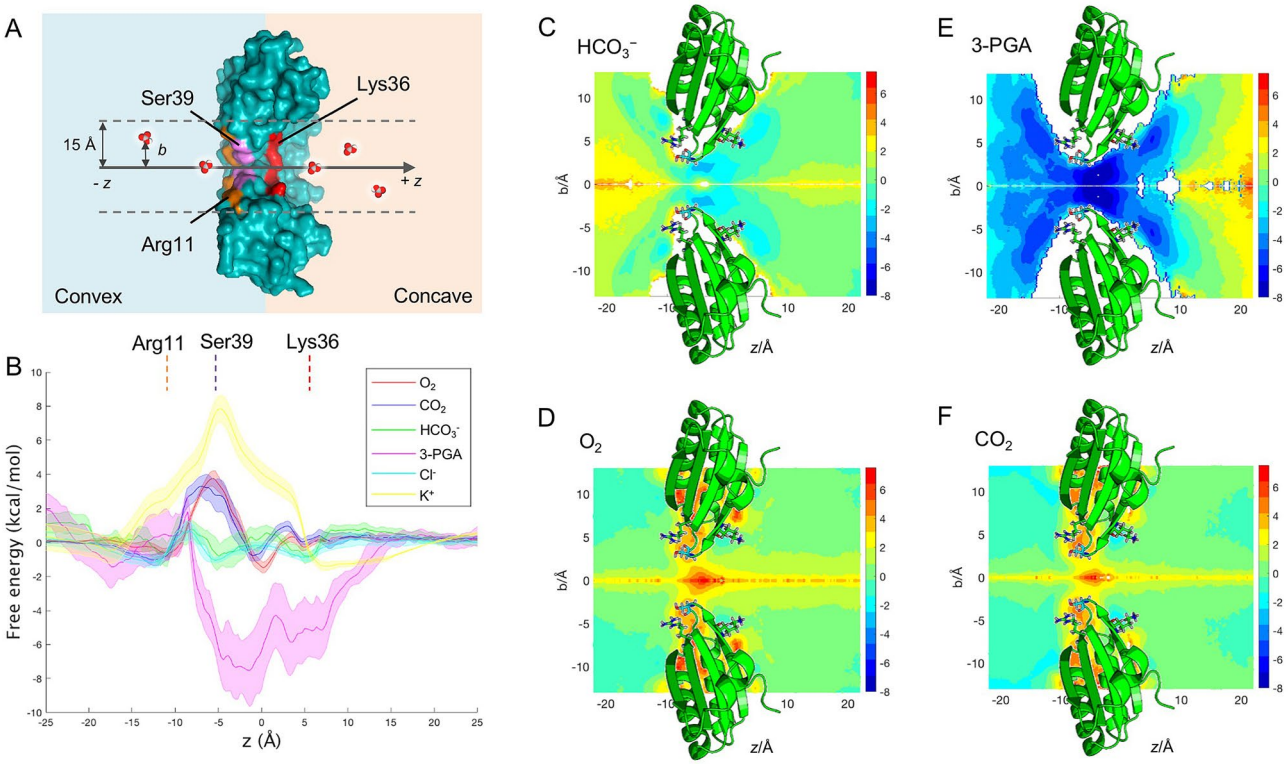

Figure 3. Selective permeability of the CcmK2-ΔC pore towards key metabolites and products related to carbon fixation. (**A**) A cross-section through a schematic representation of the US environment. The *z* axis shown is relative to (0,0,0) at the center of mass of CcmK2. The full range sampled was from −25 to +25 Å along *z*. Positive values of *z* refer to the concave side of CcmK2, whereas negative values of *z* refer to the convex surface. (**B**) Free-energy profiles of key metabolite molecules HCO_3^-, 3-PGA, O_2 and CO_2 along *z* axis, and of K^+ cations and Cl^- anions from no-metabolite control environments. (**C**–**F**) 2D free-energy landscapes of HCO_3^-, O_2, 3-PGA and CO_2 transport, respectively. A cartoon representation of CcmK2 is shown in green with the side chains of the three key residues Ser39, Lys36 and Arg11 shown as sticks.

pore, instead of creating in silico a C-terminal deletion structure based on the full-length CcmK2. Since the MD simulation lengths cannot sample the position of the flexible termini exhaustively to find a stable conformation relative to the whole protein, using the CcmK2-ΔC structure eliminates this uncertainty.

Molecular transport of the pore is mediated by electrostatic charge. The pore of CcmK2 has been proposed to be the route by which metabolites pass through the shell in either direction[22]. We conducted US simulations on CcmK2-ΔC (PDB: 3CIM) in the solvent containing HCO_3^-, 3-PGA, O_2 and CO_2, respectively. We determined the free-energy (ΔG) profiles associated with the transition of each metabolite initiating simulations in both directions, along the axis (*z*) relative to the center of mass of the CcmK2 hexamer (*x*, *y*, *z*) = (0, 0, 0) (Fig. 3A). To assess the US convergence, we divided each window into 5 equal-length trajectories to calculate the error bars, which did not display significant systematic changes (Supplementary Figure 4). We also analyzed the autocorrelation functions at 3 different US windows (Supplementary Figure 5) and obtained around 2 ns for the autocorrelation times, shorter than the US simulation lengths.

As shown in Fig. 3B, the local free energy differences are calculated relative to bulk solvent (at *z* = − 25 Å, + 25 Å). It is evident that the four metabolites experience three shared local free-energy minima/maxima, representing their specific interactions with the key amino acid residues (Fig. 3). O_2 and CO_2 have the same local free-energy minima localized around the side chains of Arg11 (*z* = ~ − 11 Å) and Lys36 (*z* = ~ 5 Å) as well as a free energy barrier, $\Delta G^{\ddagger}$ of 3.8 kcal mol^{-1} and 3.5 kcal mol^{-1} respectively, in proximity to Ser39 (*z* = ~ − 6 Å) (Fig. 3B). This indicates that both the CO_2 and O_2 have to pass a small free energy barrier to transition through the pore from one side of Ser39 to the other.

The free-energy minima of HCO_3^- are around the side chains of residues near the center of the pore, which is formed by the K-I-G-S motif[31]; Ser39 where *z* is ~ − 5 Å, Arg11 where *z* is ~ − 12 Å, and Lys36 where *z* is ~ 6 Å. The lowest of the energy wells (k_T) occurs at the Ser39 bottle neck, with a ΔG of ~ − 0.6 kcal mol^{-1}. It is the same for 3-PGA except that there is no minimum at Arg11. These free-energy minima correlate with the binding pockets of CcmK2 for metabolites in 3D space (Fig. 3C–F), indicating the importance of residues Ser39, Lys36 and Arg11 in mediating metabolite flux through the pore. Consistently, recent studies on 1,2-propanediol utilization (1,2-PDU) microcompartments have also verified the role of the equivalent Ser40 of the shell hexamer PduA in channeling metabolite traffic[32,33]. Given that the Ser39, Lys36 and Arg11 residues are conserved among

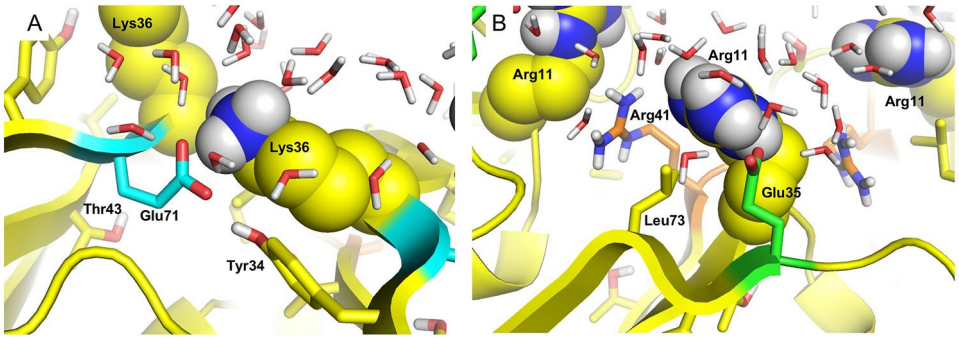

Figure 4. Interactions formed by key charged residues. Lys36 (left) and Arg11 (right) shown as van de Waals spheres at the concave and convex sides of the pore respectively. Interacting conserved Glu71 (turquoise) and Glu35 (green) residues, as well as nearby residues within 4 Å (Tyr34 and Arg41, Leu73) and water molecules are shown as sticks highlighting solvent accessibility.

orthologous BMC-H members as demonstrated by protein sequence alignment (Supplementary Figure 3)[22,27], our results may suggest a general principle underlying the selective permeability of BMC shell proteins and the conservation of functional domains of BMC shell components. Collectively, our results reveal the charge-based molecule transport through the electropositive CcmK2 pore.

Additionally, we calculated the free energy of K^+ and Cl^- using metabolite-free US simulations. The cation K^+ displays a maximum between $z = \sim -16$ to 5, with the highest ΔG of ~ 7.6 kcal mol^{-1} occurring around Ser39 $z = \sim -4$. This suggests that it is unfavorable for cations to transition through the CcmK2 pore. In contrast, the small anion Cl^- has the smoothest energy profile and is most similar to that of HCO_3^-. Overall, it experiences much smaller barrier heights for a favorable transition (Fig. 3B). The most favorable free energy occurs when 3-PGA transits around Ser39 with a ΔG of ~ −7.5 kcal mol^{-1} (Fig. 3B). This could be rationalized by the tendency for hydrogen bonds to be formed between the carboxyl group of 3-PGA and the hydroxyl group of Ser39. The local minimum of 3-PGA on the convex side is higher than around Lys36 on the concave face of CcmK2. In contrast, the local minimum of HCO_3^- around Arg11 ($z = -12$ Å) on the convex face of CcmK2 is approximately equal to the minimum around Lys36 ($z = 6$ Å) on the concave side. There is also a shared local maximum centered at $z = 0$–2 Å between the minima around Lys36 and the minima at Ser39.

These results suggest that energetically favorable interactions around and in the center of the pore increase the likelihood of transit and could drive transit of HCO_3^- and 3-PGA in both directions. It is possible that 3-PGA preferentially transits from the convex to the concave face. The energy profile suggests more favorable interactions occur on the concave side of Ser39 (Fig. 3B). While HCO_3^- US does not indicate a preference, it is likely in the cellular environment HCO_3^- would preferentially transit from the concave to the convex face with a concentration gradient. This is in agreement with the shell protein orientation characterized in the intact BMC shells[34] and the PduA nanotubes[35], but distinct from the proposed orientation in recent simulations of the α-carboxysome shell hexamer CsoS1A[36]. The pore, and the binding pockets at the key residues on either side, are accessible to water. Solvent effects, such as the likes of salinity, merit further investigation (Fig. 4, Supplementary Figure 2).

We extended the thermodynamic analysis above to the study of the dynamic characteristics associated with the transition of O_2, CO_2, and HCO_3^- molecules through the pore. We analyzed the free energy profiles obtained in Fig. 3B, within the reaction rate theory framework. Considering a constant prefactor (pre-exponential coefficient) in the Arrhenius/Kramers equation and a barrierless transition process for HCO_3^-, we measured the ratio of the rates associated with the transition of O_2 (respectively CO_2) and HCO_3^- compounds through the pore. This yields $k_{O2}/k_{HCO3-} = \sim 3.5 \times 10^{-4}$ and $k_{CO2}/k_{HCO3-} = \sim 6.6 \times 10^{-4}$, which shows significant differences (3 orders of magnitude) in terms of the characteristic times for the transition through the pore.

Conformational change of the central pore during metabolite transit. To examine whether potential conformational changes of the CcmK2 pore are associated with transit of metabolites, we measured the pore diameter in the presence and absence of contacts between individual metabolites and the residues Arg11, Ser39 and Lys36 during the time course of simulations (Fig. 5), using HOLE[37] to analyze 2500 equidistant frames of a 50 ns MD trajectory independently (see Materials and methods). The pore size of CcmK2-ΔC in the crystal structure (PDB: 3CIM) was 2.55 Å determined using HOLE, and it varied between 1 and 6 Å during the course of simulations (Fig. 5). There were no significant differences found in the pore diameter in the absence and presence of contacts between CO_2 or O_2 and the three residues. It is worth noting that the sample size of contacts between these metabolites and the select residues is small, likely because the substrates with relatively small size have more space to move freely in the pore area without making contacts. On the contrary, a significant difference in the pore size was discerned for HCO_3^- between no contacts and contacts with Lys36 (Fig. 5, Supplementary Table 2). This reveals that transit of HCO_3^- may first require binding to Lys36 on the concave side of the protein to open up the pore. Significant changes in the pore diameter were also detected in the presence and absence of contacts between 3-PGA and all three of the selected residues of interest, indicating that the passage of 3-PGA through the pore may require a conformational change to increase the pore diameter (Fig. 5).

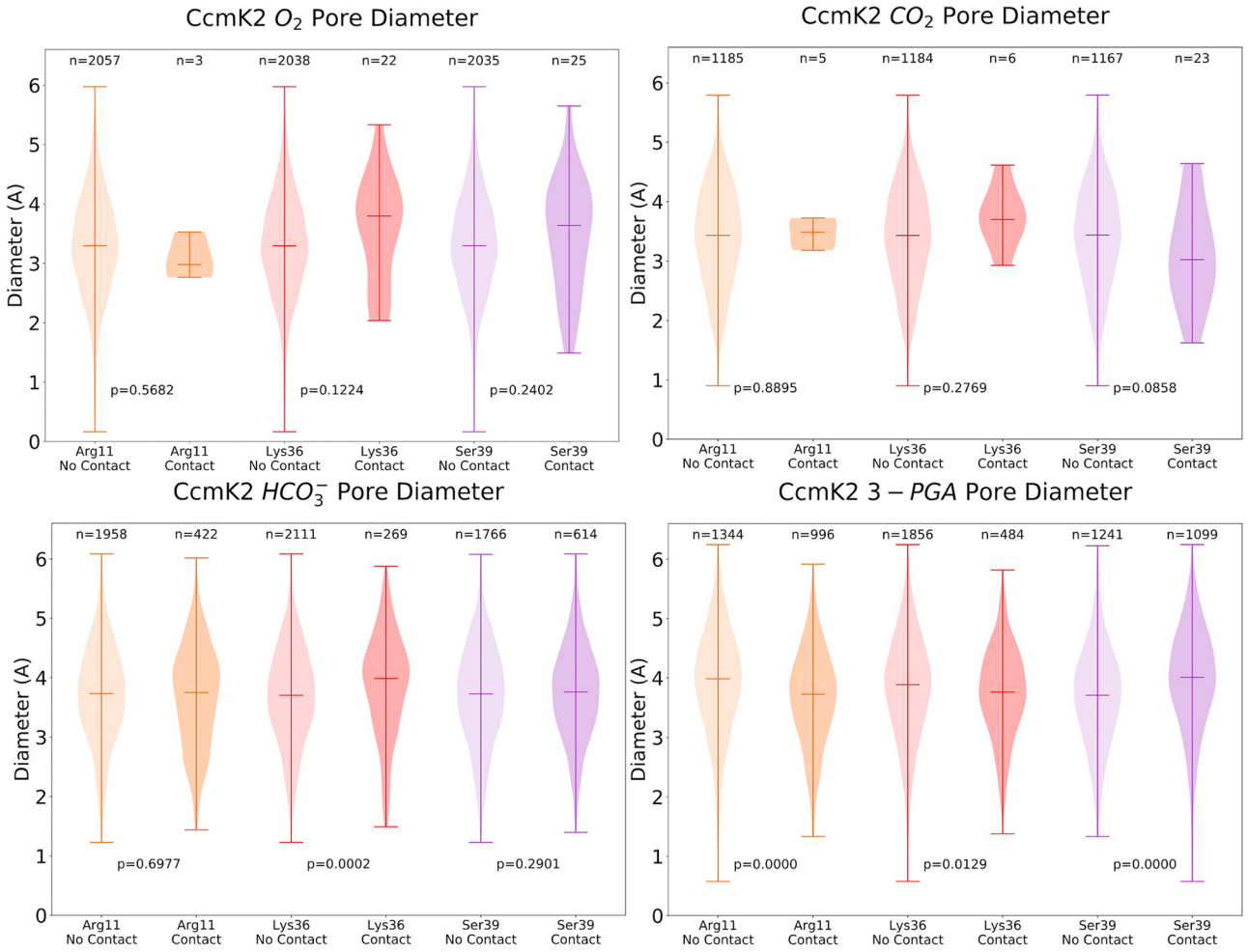

Figure 5. Pore diameter of CcmK2-ΔC in the presence and absence of contacts with metabolites during simulations. Violin plots of the pore diameters of CcmK2 determined by HOLE from the full MD simulations trajectories for each metabolite, depicting the conformational dynamics of the pore during metabolite transition. The two categories "contact" and "no contact" refer to the presence or absence, respectively, of the metabolite within the cutoff distance of 3.5 Å and angle of 30° of the reside. *p* values were calculated using the Wilcoxon rank-sum test (Supplementary Table 2). These diameter measurements were made at the region corresponding to the minimum constriction along the pore axis *z*.

Permeability of large metabolite molecules through the CcmK2 pore. Our results imply that the large molecule 3-PGA experiences favorable interactions (Fig. 3B) and may induce a conformational change of the CcmK2 pore during transit (Fig. 5). Likewise, RuBP also has a large size (~3–4 Å wide, ~9.4 Å long) with respect to the pore diameter (Fig. 6A). We calculated the acidic dissociation constants based on the Hammett and Taft equations using the Epik method (black) and empirically calculated physico-chemical parameters obtained from ionization site-specific regression equations (red) annotated on Fig. 6A. The pKa calculations exhibited consistency regardless of the pKa calculation methods, suggesting the most likely protonation state of RuBP and 3-PGA molecules at ~pH7.

To estimate their interactions with the CcmK2 pore, we conducted molecular docking simulations of 3-PGA and RuBP with CcmK2-ΔC structure using SwissDock[38] and Glide extra precision (XP) docking[39]. Snapshots of the most stable binding poses for RuBP (Fig. 6B) and 3-PGA (Fig. 6C) from both the concave and convex faces illustrate the negative relative free energy changes experienced by RuBP and 3-PGA when in the final docking pose in the CcmK2 pore: Δ*G* is -9.96 kcal·mol^{-1} for RuBP (Fig. 6D) and −9.98 kcal·mol^{-1} for 3-PGA (Fig. 6E). The FullFitness score for RuBP (−3383 kcal mol^{-1}) in this pose is similar to 3-PGA (−3275 kcal mol^{-1}) (Supplementary Figure 6). These results verify a highly stable binding pocket for 3-PGA and RuBP in the narrowest point of the CcmK2 pore when the phosphate groups of these metabolites interact with the Ser39 hydroxyl groups. All three of the phosphate oxygen groups of both RuBP and 3-PGA can be stabilized by hydrogen bonding to Ser39. This binding pocket also contributes to a local free-energy minimum for 3-PGA, as observed in US calculations ($z = \sim -5$ Å) (Fig. 3). This emphasizes a good correlation between our molecular docking and US simulations results, despite the known lower reliability of docking simulations compared to full MD simulations. These binding poses of 3-PGA are directly compared between US and docking in Fig. 7. Interestingly, despite the size

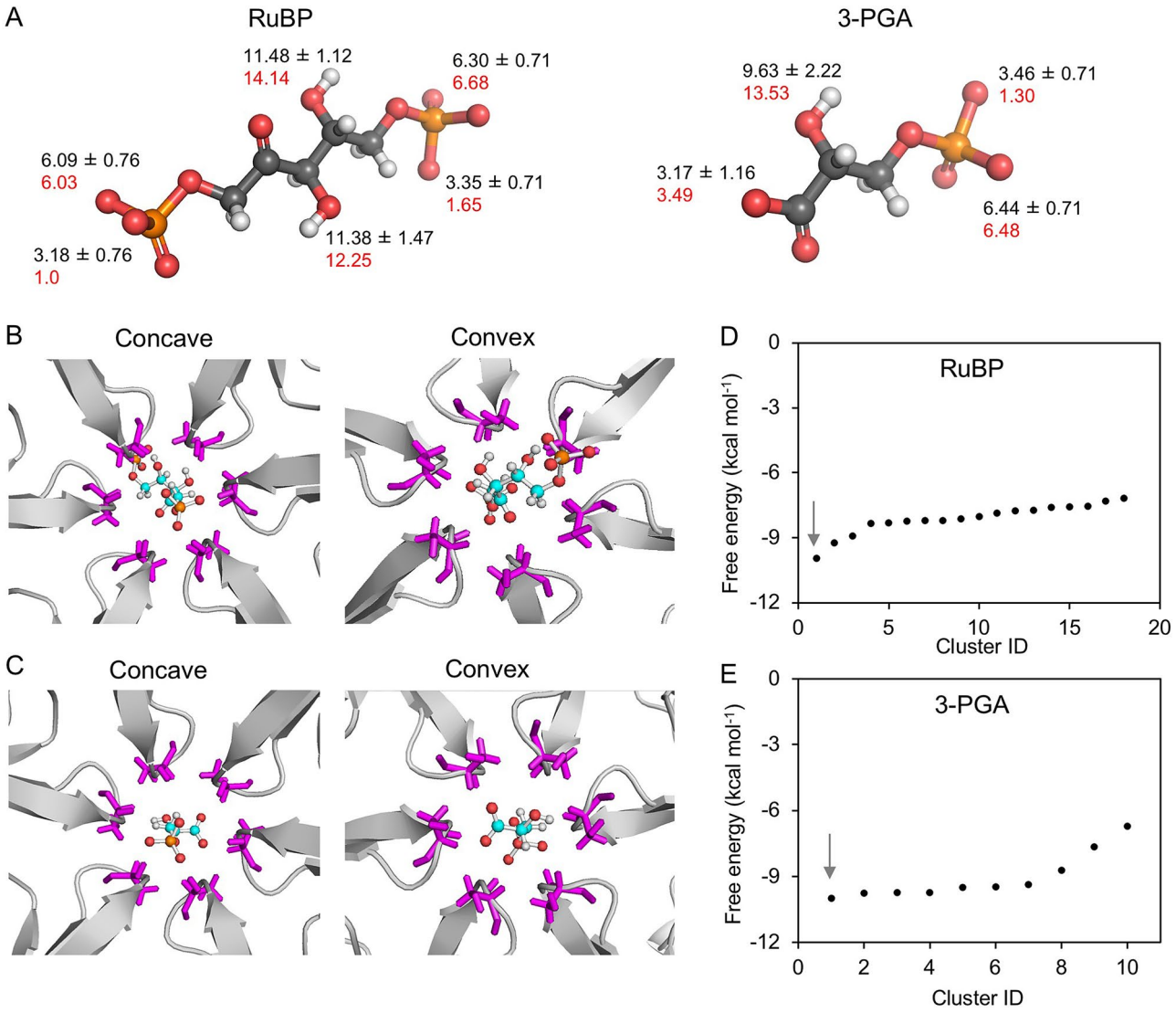

Figure 6. Interactions of large metabolites RuBP and 3-PGA with CcmK2-ΔC. (**A**) Ball-and-stick representation of the most likely protonation state of RuBP and 3-PGA molecules at ~ pH7. The acidic dissociation constants calculated based on the Hammett and Taft equations using the Epik method (black) and empirically calculated physico-chemical parameters obtained from ionization site-specific regression equations (red) are shown. (**B**) Interactions of RuBP with the Ser39 residues (purple) displayed from concave and convex sides, hydrogen bonding between the phosphate oxygens and Ser39 side chain indicated by dotted lines. (**C**) Interactions of 3-PGA with the Ser39 residues (purple) displayed from concave and convex sides. (**D**) Free energy scores of clustered RuBP binding positions. The interaction site shown in (**B**) bears the minimal free energy in Cluster ID 1, as indicated by the arrow. (**E**) Free energy scores of clustered 3-PGA binding positions. The interaction site shown in (**C**) has the minimal free energy in Cluster ID 1, as indicated by the arrow. The results suggest that the most stable interacting sites with RuBP and 3-PGA are both on the convex side of CcmK2. The docking snapshots show the fully deprotonated form of RuBP and 3-PGA. These may be other protonation states of these molecules within the pore, which are not represented in this figure for simplicity.

difference between 3-PGA and RuBP, the free energy detected when docking RuBP and 3-PGA to CcmK2 is relatively similar. This might suggest that there are relatively strong interactions between the binding pocket and RuBP or 3-PGA. This binding pocket is alike for both molecules, but accessibility is equally challenging due to the small diameter of the pore and large sizes of the metabolites. As the binding poses observed are solvent-accessible and make use of the charged phosphate groups of the metabolites bound in the polar center of the pore, we do not expect significant changes in their protonation states upon binding. Nevertheless, a significant change in pH that affects the protonation states of these metabolites might result in the changes in binding energies and poses.

Effects of pore mutation on in vivo physiology. Our simulation results suggest that the Ser39 residue in CcmK2 is a key residue in the charged-based mechanism that mediates the flux of metabolites into and out of the carboxysome. To corroborate the in-silico findings, we investigated the significance of Ser39 on

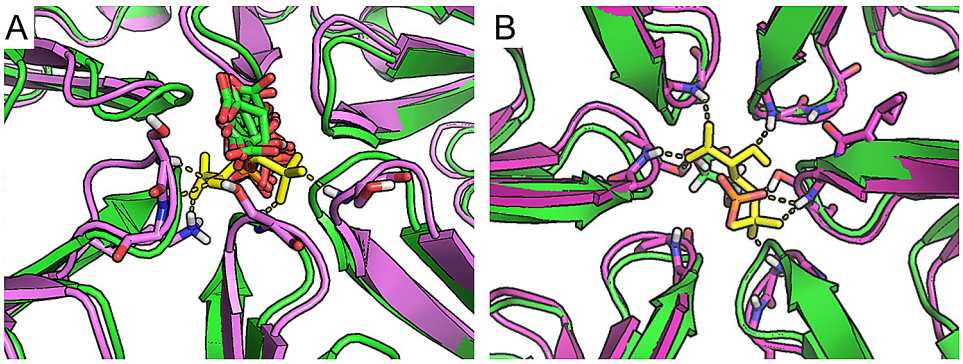

Figure 7. Comparison of docking and US MD poses of 3-PGA. (**A**) View from the concave side, docking poses (green cartoon for protein and sticks for 3-PGA) compared with 3-PGA bound structures at the free energy minimum from US MD simulations (3-PGA: yellow sticks, protein: purple cartoon). Note that more extended hydrogen bonds can form due to small rotations of the loops at the center of the pore, allowing interactions of 3-PGA with Ser backbones, Lys and Ser sidechains (shown as sticks). (**B**) Comparison between top docked pose (green cartoon for protein and sticks) and selected MD snapshot from the free energy minimum (purple cartoon and yellow sticks).

carboxysome activities and cell physiology by constructing a CcmK2-S39A point mutation. The carboxysome of Syn6803 in addition to CcmK2 contains another major shell protein CcmK1[21], whereas in Syn7942, CcmK2 proteins act as the only major shell components in the carboxysome shell, as shown by a previous proteomic study[40]. The CcmK2 proteins of Syn7942 and Syn6803 present a high sequence similarity and the Ser39 residues are highly conserved (Supplementary Figure 3). To prevent the complementary effects of CcmK1, whose role is still unclear, we generated the CcmK2-S39A mutant in Syn7942 and examined cell growth and carbon fixation activities of the Syn7942 mutants including knockouts of the other shell proteins.

We compared the growth of CcmK2-S39A in three conditions: air, $NaHCO_3$ supplemented, and 4% CO_2. The CcmK2-S39A strain could grow at 4% CO_2, with a similar growth rate with WT (Fig. 8A). By contrast, the growth of CcmK2-S39A was greatly impeded under the air and HCO_3^- supplemented conditions, compared with those of WT under the same conditions (Fig. 8B). This raises the possibility that the S39A mutation may preclude transport of bicarbonate into carboxysomes, or prevents other functions of the pore, such as luminal CO_2 retention. We also determined that the distinct carbon-fixation activities of the WT and CcmK2-S39A cells grown under 4% CO_2 (Fig. 8C). CcmK2-S39A has a lower apparent V_{max} (10.0 ± 1.5 μmol·min^{-1}·OD^{-1}, $n = 4$) and a higher $K_{m(\mathrm{RuBP})}$ (1.7 ± 0.6 mM, $n = 4$) compared with the WT ($V_{max} = 28.3 \pm 2.0$ μmol·min^{-1}·OD^{-1}, $K_{m(\mathrm{RuBP})} = 0.7 \pm 0.4$ mM, $n = 4$), revealing the affected Rubisco activity caused by the pore mutation. The increased RuBP binding affinity $K_{m(\mathrm{RuBP})}$ might act as a physiological adaption to compensate for a decreased propensity of RuBP transit into the carboxysome, especially at a low concentration of RuBP.

We further generated the CcmK2-S39A mutation in Δ*ccmK3*, Δ*ccmK4*, Δ*ccmK3K4* and Δ*ccmP* Syn7942 strains, respectively. It is evident that CcmK2-S39A had a notable influence on the growth of all these strains in the air and HCO_3^- supplemented conditions and resulted in a detectable reduction in carbon-fixation activity (Supplementary Figure 7). The effects of point mutations of CcmK2 Arg11 and Lys36 residues on shell permeability merit further investigation.

Discussion

Selective permeability of the carboxysome shell allows the generation of a local microenvironment with an optimized luminal concentration of metabolites, crucial for carbon assimilation of this specialized organelle. In particular, the carboxysome shell was proposed to facilitate the diffusion of HCO_3^- and probably provides a barrier to O_2 and reduces CO_2 leakage into the cytosol[41], and thus, plays roles in minimizing the unproductive oxygenation and improving the carboxylation of Rubisco encased by the carboxysome shell. The shell is also permeable to protons, leading to similar pH conditions in the carboxysome compartment lumen and the cytoplasm[42]. Here, we conducted a systematic characterization of the principles underlying the permeability of the major carboxysome shell protein CcmK2[12], using an array of computational approaches. Our study suggests that the mechanism of metabolite transit through the CcmK2 pore represents a combination of electrostatic charge-based transition and the conformational change of the pore. Our simulations results, combined with the recent findings which have demonstrated that the concave surfaces of shell proteins in the uniformly-oriented shell[25] face out of the BMC[34,35], allow us to propose a model for the metabolite flux across the carboxysome shell (Fig. 9). This may be dependent on the protonation states of both the metabolites and amino acid side chain residues in the pore. In different protonation states under distinct pH conditions, transition of metabolites through the pore may vary. It is likely that carboxysomes in the cytoplasm exist exclusively at close to neutral pH due to homeostasis, regardless of the external pH[43]. At pH = ~7, the metabolites characterized here may exist as an ensemble of protonation states; for example, bicarbonate ions will exist as both carbonic acid and hydrogen carbonate. These two protonation states may bind and dock differently inside the pore of CcmK2. This is an

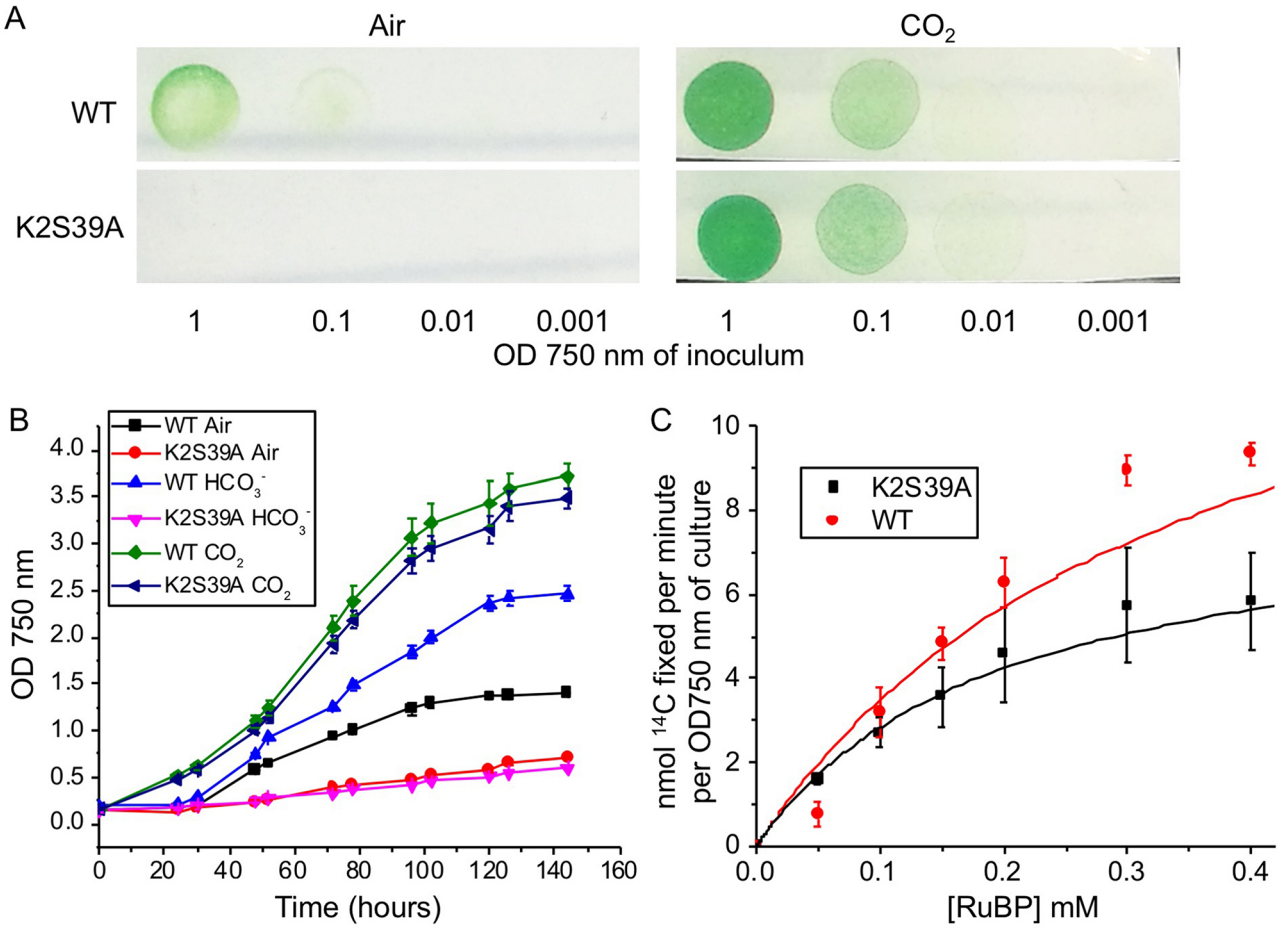

Figure 8. Physiology of the Syn7942 WT and CcmK2-S39A mutant. (**A**) Growth of WT and CcmK2-S39A strains under air or 4% CO_2. A series of dilutions from liquid cultures with OD750 of 1 were plated on BG11 plates and imaged after 48 h. (**B**) Growth curves of WT and CcmK2-S39A cells in air, 4% CO_2, or with daily 150 mM HCO_3^- supplements. Growth of three biological repeats ($n = 3$) was recorded. CcmK2-S39A requires high CO_2 to survive, grow slowly in air, and with HCO_3^- supplements. (**C**) Carbon fixation activities of WT and CcmK2-S39A (OD750 = 1) as a function of RuBP dosage, fitted with Michaelis–Menten curves ($n = 4$). CcmK2-S39A has a lower V_{max} (10.0 ± 1.5 μmol·min^{-1}·OD^{-1}) and a higher K_m (1.7 ± 0.6 mM) compared with WT ($V_{max} = 28.3 \pm 2.0$ μmol·min^{-1}·OD^{-1}, $K_m = 0.7 \pm 0.4$ mM).

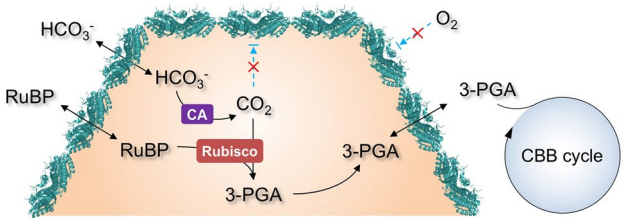

Figure 9. Schematic model representing the selective permeability of the carboxysome shell to confine metabolite flux for driving the CBB cycle. CcmK2 hexamers are the major components in the icosahedral carboxysome shell, with the concave side facing outwards to the cytoplasm and the convex side facing inwards to the lumen. Based on the positive electrostatic charge of the central pore, CcmK2 acts as a tunnel for HCO_3^- influx and a barrier to O_2 and CO_2, precluding O_2 influx and leakage of CO_2 from the carboxysome lumen to the cytoplasm. Larger molecules RuBP and 3-PGA can likely pass through CcmK2 but require a conformational change in the CcmK2 pore involving a flip of the Ser39 side chain.

important consideration for both the result interpretation in this work and for future studies, which may require constant pH simulations[44,45] that were outside the scope of this study.

We show that the selective permeability of CcmK2 is dependent on the electrostatic charges of molecules. It is energetically favorable for the negatively charged HCO_3^- to move through the pore, but less favorable for CO_2 and O_2 to pass through the pore, akin to the experimental findings[41,46]. This is of physiological significance for improving carbon fixation. Bicarbonate represents the dominant fraction of carbon dioxide in the aqueous cyanobacteria-growing environment and the cytoplasm. It is pumped across the cytoplasmic membranes of cyanobacteria into the cytoplasm by HCO_3^- transporters, resulting in a great accumulation of bicarbonate within the cell to a level up to 1000-fold higher than exogenous bicarbonate[47]. The cytosolic HCO_3^- then passes across the shell and is converted to CO_2 by CA that is co-encapsulated with Rubisco within the carboxysome (Fig. 9), leading to elevated levels of CO_2 close to Rubisco to favor the carboxylation activities of Rubisco. Although free-energy simulations could not define explicitly the preferable direction of HCO_3^- transit through the pore (Fig. 3), the HCO_3^- gradient across the shell (a high level of HCO_3^- outside the shell and a falloff of the HCO_3^- level within the compartment in the presence of CA) may play the decisive role in driving the flow of HCO_3^- into the carboxysome. In addition, both transits of CO_2 and O_2 through the pore were revealed to be energetically unfavorable (Fig. 3). This suggests that the shell predominately composed of CcmK2 may act as a barrier to CO_2 leakage from the carboxysome into the cytosol, as well as O_2 influx into the carboxysome, therefore facilitating the CO_2-fixing activities and diminishing the oxygenation of Rubisco. From the present computational data alone, it is hard to conclude to what extent the transition of O_2 and CO_2 through CcmK2 is blocked. Further simulation data and validation of the force field with particular respect to hydration free energies and partition coefficients are required to investigate the extent of the exclusion of O_2 and the retention of CO_2.

This mechanism of metabolite transit through the pore described in this study may be applicable to not only β-carboxysomes but also α-carboxysomes, based on the recent simulations study on the α-carboxysome shell protein CsoS1A and the β-carboxysome shell protein CcmK4[36]. Moreover, experimental studies have suggested that the α-carboxysome shell could impede the entrance of CO_2 into the carboxysome[41] and obviate its loss from the carboxysome lumen[46].

Transit of the relatively large metabolites, such as 3-PGA and RuBP, through the pore of CcmK2 is potentially challenging. It remains to be tested whether it is possible for small molecules, or larger metabolites, or both, to move through the space between adjoining CcmK hexamers. Though the 3-PGA transit is energetically favorable (Fig. 3), it could induce a detectable conformational change of CcmK2 (Fig. 5). Given that RuBP is larger than 3-PGA, the RuBP transit through the CcmK2 pore is presumably more difficult. By contrast, the pseudo-hexamer CcmP, another shell protein in the β-carboxysome, bears a larger central pore (~ 13 Å) compared with CcmK2[48,49]. It may act as a conduit for large metabolites, as a 3-PGA molecule may fit the pore of CcmP[49] and a glycerol molecule has been observed in a binding pocket of the CcmP open structure[48]. The mechanism that controls RuBP and 3-PGA transit through the shell awaits further investigation. Moreover, cations, like Mg^{2+} that are required in the active site of Rubisco, may not be able to pass through the central pore of CcmK2 as easily as these large metabolites. It remains to be tested whether cations could transit through the CcmK2 pore or the pores of other shell proteins i.e. CcmK3, CcmK4 and CcmL, or through the gaps surrounding shell proteins generated by specific protein arrangement[34] and dynamic self-assembly and interactions[25,50].

Simulations revealed a 1–6 Å variation in the pore size of CcmK2 during metabolite passage (Fig. 5). This conformational change consists primarily of the loops forming the central pore region twisting, and the rotation of the Ser39 side chains into and away from the center of the pore. Greater variations in the pore size of shell proteins have been characterized in the open and closed forms of the pseudo-hexamers CcmP[48], CsoS1D[51], and EutL[52]. This suggests that pore conformational change could provide a means for selective metabolite transport (especially for large metabolite molecules) of shell proteins in the BMC counterparts. There was a distinct phenotype for each knockout mutant (Fig. 8, Supplementary Figure 7). This may also suggest that there may be distinct roles for each shell protein or at least each class of BMC-T, BMC-P and BMC-H proteins, including the transit of the larger metabolites.

The rise of synthetic biology has spurred bioinspired engineering of BMC-based organelles for biotechnological applications, such as novel metabolic factories and molecule scaffolds, in light of the self-assembly, encapsulation and modular nature of BMC structures. Manipulating shell permeability is a pivotal strategy for design and construction of new BMCs to direct molecular transport and favor specific metabolic reactions. This study indicates that the mechanism controlling the permeability of the shell is complex and may be different between the different types of BMC as well as between the alpha and beta carboxysomes. The conserved residues of shell proteins that are vital for tuning the pore permeability, especially Ser39 of CcmK2, could be important targets in bioengineering to fine-tune molecular passage through beta-carboxysome shell structures. This study provides a predictive methodology to gain a more complete biophysical understanding of the mechanistic basis underlying molecular passage through the carboxysome shell. A deeper knowledge of the permeability of BMC shell proteins will inform strategies for the design and construction of new BMC-based nanoreactors to improve cell metabolism.

Materials and methods

Cell culture and construction of genetic mutants. Syn7942 cultures were grown at 30 °C under constant white light illumination of 30 $\mu E \cdot m^{-2}\ s^{-1}$, in BG11 medium[53]. Cultures were under one of three conditions, "Air"—atmospheric condition, "HCO_3^-"—BG11 supplied with $NaHCO_3$ in every 24 h to reach a final concentration of 150 mM, and "CO_2"—4% CO_2 supplied in air. Cell growth was monitored at OD = 750 nm by a spectrophotometer (Jenway 6300). BG11 was supplemented with 10 mM TES buffer to increase its buffering

capacity and minimize pH changes due to $NaHCO_3$ addition[54]. *E. coli* cultures were grown at 37 °C with constant shaking in Luria-Broth (LB).

Point mutation of CcmK2 (CcmK2-S39A) from Syn7942 was generated using the In-Fusion® approach in DH5α *E. coli*. Plasmids containing *ccmK2-S39A* and a kanamycin resistance cassette were transformed into Syn7942 cells to replace the native *ccmK2* gene in the genome, using Lambda RED Recombination[55] as described previously[56–59]. Syn7942 knockout mutants Δ*ccmK3*, Δ*ccmK4*, Δ*ccmK3K4* and Δ*ccmP* were generated in a similar fashion by replacing the gene with a spectinomycin resistance cassette. Segregation of recombinant genes was verified by PCR and agarose gel electrophoresis. Mutants were selected for by the addition of 100 μg mL^{-1} kanamycin or spectinomycin where appropriate.

Rubisco activity assays. In vivo carbon fixation from $NaH^{14}CO_3$ to ^{14}C 3-PGA was monitored as previously described[11,59]. In brief, Syn7942 cells were incubated at 30 °C with 25 mM $NaH_{14}CO_3$ for 2 min before permeabilization with 0.03% (w/v) mixed alkyltrimethylammonium bromide (Sigma-Aldrich) and RuBP (Sigma-Aldrich) was then added to initiate the reaction. The reaction was terminated after 5 min and radioactivity measurements were carried out using a scintillation counter (Tri-Carb; Perkin-Elmer). Four biological repeats were prepared for each strain used in the kinetic analysis. Data processing was performed using SigmaPlot and figures were prepared using Origin.

Crystal structure preparation. The full-length CcmK2 structures (PDB: 2A1B, 4OX7)[22,28] and the CcmK2 C-terminal deletion structure (PDB: 3CIM)[27] were obtained from the Protein Data Bank. Atoms in the unassigned regions of electron density maps of PDB structures were assigned manually and potential rotamers were fixed to a single conformation manually. Coot[60,61] was used to view the electron density map and replace missing atoms and rotamers with our inferred most likely conformation.

NAMD MD and US simulations. Umbrella sampling (US) molecular dynamics (MD) simulations were performed with the NAMD 2.12 program[62] using the CHARMM36 force field (FF)[63], to explore the passage of metabolites across the narrow central pore. Each system was built up using the CHARMM-GUI webserver[64] and the ligands (HCO_3^-, CO_2, O_2 and 3-PGA) were automatically parameterized with CGenFF using their equilibrium structures obtained with the Gaussian 09 program package[65] at the B3LYP/Def2-TZVP + GD3 level of theory. The protonation state of 3-PGA was chosen according to the microspecies distribution at pH = 7 predicted by the MarvinSketch software of ChemAxon. CcmK2-ΔC cyclic hexamer and the ligands were solvated in a hexagonal prism TIP3 water box of height 70 Å, then chloride ions were added to 0.15 M, and potassium ions were added to neutralize the system. For each system, corresponding to the four different types of metabolites, 10 molecules were randomly placed in the simulation box.

The MD protocol consisted of the following steps: (a) energy minimization over 2500 steps; (b) equilibration over 2 ns at constant pressure and temperature ($p = 1.01325$ bar, $T = 303.15$ K) with a root-mean-square deviation (RMSD) constraint of 1.0 kcal·mol^{-1}·$Å^{-2}$ applied on the protein backbone atoms; (c) 2 ns run in the NPT ensemble without constraints; (d) steered molecular dynamics (SMD) simulation—to obtain the starting positions for the subsequent umbrella sampling (US) simulations—with a pulling velocity of 10 Å ns^{-1}, and SMD force of 7 kcal·mol^{-1}·$Å^{-2}$ applied on all heavy atoms of the small molecule; (e) 10 ns US production runs for each umbrella window in the NPT ensemble. Trajectories were run with a time step of 2 fs and the collective variables employed in US simulations were printed out in each step and used for the analysis. Constant temperature was set by a Langevin thermostat with a thermostat damping coefficient of 1 ps^{-1} with a collision frequency of 5 ps^{-1}[65]. All of the bonds and angles involving hydrogen atoms were constrained by the SHAKE algorithm[65]. We used the particle mesh Ewald method[66] for the long-range electrostatics in combination with a 12 Å cutoff for the evaluation of the non-bonded interactions.

The collective variable used as reaction coordinate (z) to describe the passage of ligands is defined as the projection of the molecule's center of mass to the z-axis passing through the center of the pore (the positive z values correspond to the concave side of the protein). For each small molecule, 105 umbrella windows were run at steps of 0.5 Å ($-26.0 \leqslant z \leqslant 26.0$ Å) using a spring constant of 5.0 kcal·mol^{-1} $Å^{-2}$. Moreover, the motion of the small molecule was constrained to the interior of a cylinder centered to the z-axis with $z_{min} = -28$ Å and $z_{max} = 28$ Å, whereas the maximum of the radial distance (b) from the z axis set to 15 Å. In case of Cl^- and K^+ ions, 4 and 7 ions were selected in the cylinder, respectively by taking into account the $V_{cylinder}/V_{simulation\ box}$ ratio and concentration of ions. Their motion was completely free inside the cylinder (i.e. no umbrella bias applied) defined above and their trajectories interpreted as independent simulations during analysis. The free energy profiles and surfaces of substrate passage through the BMC pore, 1D(z) and 2D(z,b), were obtained using the weighted histogram analysis method (WHAM)[67,68], and the dynamic histogram analysis method (DHAM)[68], respectively. The mean and standard error for the 1D(z) free energy profiles were obtained by dividing the simulations for each US window into 5 equal-length segments, and analyzed these independently.

Molecular dynamics and molecular docking simulations. Gromacs[69] was used to perform 200 ns MDs of CcmK2-ΔC and CcmK2-full (PDB: 2A1B and 4OX7). All atom simulations were carried out in the GROMACS v2018.1 package with the CHARMM36 force field[63] and the TIP3P model for the explicit solvent model. The leapfrog integrator was used to integrate the equations of motion every 2 fs. To restrict bond lengths the LINCS algorithm and PME with a real space cut-off at 14 Å were applied. RMSD was calculated by least square fitting of the protein to the crystal structure and then calculating the pairwise RMSD at each time step. RMSD was calculated for the entire hexamer assembly to take structural drift of the assembly in whole into con-

sideration. Per residue RMSF were calculated for each chain and plotted as boxplots, to compare the flexibility of the three CcmK2 structures.

Two sets of independent docking simulations were carried out in SwissDock[38] and Glide[39], to characterize the binding poses of RuBP and 3-PGA with the 3CIM structure. Binding poses were scored using their FullFitness and clustered. Clusters were then ranked according to the average FullFitness of their elements[70].

The acidic dissociation constants of the 3-PGA molecule were obtained with (1) the Epik method, based on the Hammett and Taft equations, as performed in the Schrödinger 2020-3 software (https://www.schrodinger.com/), and (2) based on empirically calculated physico-chemical parameters obtained from ionization site-specific regression equations, as performed in the Marvin 17.21.0 software ChemAxon (https://www.chemaxon.com). The structures of RuBP and 3-PGA molecules were prepared using Pymol (https://www.pymol.org).

Determining the pore diameter during metabolite flux. CPPTRAJ[71] from Amber[72] was used to align the trajectory files to the reference structure of CcmK2 (PDB: 3CIM) using the RMSD of alpha carbon atoms. The trajectories were then split into individual PDB files for each time frame. HOLE[37] was used to measure the radius of the pore and given as an output of the diameter. This procedure was run for every timeframe that was split from the trajectory. These diameter measurements were made at the region corresponding to the minimum constriction along the pore axis z. VMD was used to find all the contacts, within a cutoff distance of 3.5 Å and angle of 30°, between each metabolite and the residues Arg11, Ser39 and Lys36. The number of contacts with each residue in each time frame was recorded. The pore diameter data was split into two categories, "no contact" when the metabolite did not fall within the cutoff of the specified residue, and "contact" when 1 or more contacts occurred. P values were calculated using the Wilcoxon rank-sum test from the SciPy python library, and violin plots were produced using Matplotlib.

Autocorrelation analysis. To estimate the 2D-surface area of the pore, we defined a hexagon via the Ser39 CA atoms of the 6 loops defining the pore entrance that lie approximately on a plane (Supplementary Figure 5A). We triangulated the hexagon via its vertices using a Delaunay Triangulation, and estimated the surface area as the sum of the areas of the triangles. We considered representative configurations from 3 US windows along the z axis when the metabolite is located at $z = -20$ Å, $z = -5$ Å, and $z = 20$ Å. The autocorrelation time, τ, associated with the temporal evolution of the pore surface area of CcmK2 from the US trajectories for the metabolites was measured for the selected US windows (Supplementary Figure 5B).

Protein sequence alignment. The protein sequences of shell hexamer homologs were taken from KEGG (https://www.genome.jp/kegg/) and the alignment was conducted using Clustal Omega.

Computational resources. The computational work for this article was partially performed on resources of the National Supercomputing Centre, Singapore, the Chadwick Cluster, Advanced Research Computing, the University of Liverpool and ARCHER, the UK National Supercomputing Service.

Received: 24 June 2019; Accepted: 29 September 2020
Published online: 15 October 2020

References

1. Bobik, T. A., Lehman, B. P. & Yeates, T. O. Bacterial microcompartments: widespread prokaryotic organelles for isolation and optimization of metabolic pathways. *Mol. Microbiol.* **98**, 193–207 (2015).
2. Kerfeld, C. A., Aussignargues, C., Zarzycki, J., Cai, F. & Sutter, M. Bacterial microcompartments. *Nat. Rev. Microbiol.* **16**, 277–290 (2018).
3. Kerfeld, C. A. & Erbilgin, O. Bacterial microcompartments and the modular construction of microbial metabolism. *Trends Microbiol.* **23**, 22–34 (2015).
4. Yang, M. *et al.* Decoding the stoichiometric composition and organisation of bacterial metabolosomes. *Nat. Commun.* **11**, 1976 (2020).
5. Yeates, T. O., Thompson, M. C. & Bobik, T. A. The protein shells of bacterial microcompartment organelles. *Curr. Opin. Struct. Biol.* **21**, 223–231 (2011).
6. Badger, M. R. & Price, G. D. CO_2 concentrating mechanisms in cyanobacteria: molecular components, their diversity and evolution. *J. Exp. Bot.* **54**, 609–622 (2003).
7. Cannon, G. C. *et al.* Microcompartments in prokaryotes: carboxysomes and related polyhedra. *Appl. Environ. Microbiol.* **67**, 5351–5361 (2001).
8. Yeates, T. O., Kerfeld, C. A., Heinhorst, S., Cannon, G. C. & Shively, J. M. Protein-based organelles in bacteria: carboxysomes and related microcompartments. *Nat. Rev. Microbiol.* **6**, 681–691 (2008).
9. Huang, F. *et al.* Rubisco accumulation factor 1 (Raf1) plays essential roles in mediating Rubisco assembly and carboxysome biogenesis. *Proc. Natl. Acad. Sci. U. S. A.* **117**, 17418–17428 (2020).
10. Rae, B. D., Long, B. M., Badger, M. R. & Price, G. D. Functions, compositions, and evolution of the two types of carboxysomes: polyhedral microcompartments that facilitate CO_2 fixation in cyanobacteria and some proteobacteria. *Microbiol. Mol. Biol. Rev.* **77**, 357–379 (2013).
11. Faulkner, M. *et al.* Direct characterization of the native structure and mechanics of cyanobacterial carboxysomes. *Nanoscale* **9**, 10662–10673 (2017).
12. Sun, Y., Wollman, A., Huang, F., Leake, M. & Liu, L. Single-organelle quantification reveals the stoichiometric and structural variability of carboxysomes dependent on the environment. *Plant Cell* **31**, 1648–1664 (2019).
13. Bracher, A., Whitney, S. M., Hartl, F. U. & Hayer-Hartl, M. Biogenesis and metabolic maintenance of Rubisco. *Annu. Rev. Plant Biol.* **68**, 29–60 (2017).

14. Kerfeld, C. A. & Melnicki, M. R. Assembly, function and evolution of cyanobacterial carboxysomes. *Curr. Opin. Plant Biol.* **31**, 66–75 (2016).
15. Behrenfeld, M. J. *et al.* Biospheric primary production during an ENSO transition. *Science* **291**, 2594–2597 (2001).
16. Fang, Y. *et al.* Engineering and modulating functional cyanobacterial CO_2-fixing organelles. *Front. Plant Sci.* **9**, 739 (2018).
17. Bonacci, W. *et al.* Modularity of a carbon-fixing protein organelle. *Proc. Natl. Acad. Sci. U. S. A.* **109**, 478–483 (2012).
18. Lin, M. T., Occhialini, A., Andralojc, P. J., Parry, M. A. J. & Hanson, M. R. A faster Rubisco with potential to increase photosynthesis in crops. *Nature* **513**, 547–550 (2014).
19. Lin, M. T. *et al.* β-Carboxysomal proteins assemble into highly organized structures in Nicotiana chloroplasts. *Plant J.* **79**, 1–12 (2014).
20. Occhialini, A., Lin, M. T., Andralojc, P. J., Hanson, M. R. & Parry, M. A. Transgenic tobacco plants with improved cyanobacterial Rubisco expression but no extra assembly factors grow at near wild-type rates if provided with elevated CO_2. *Plant J.* **85**, 148–160 (2016).
21. Tanaka, S. *et al.* Atomic-level models of the bacterial carboxysome shell. *Science* **319**, 1083–1086 (2008).
22. Kerfeld, C. A. *et al.* Protein structures forming the shell of primitive bacterial organelles. *Science* **309**, 936–938 (2005).
23. Lassila, J. K., Bernstein, S. L., Kinney, J. N., Axen, S. D. & Kerfeld, C. A. Assembly of robust bacterial microcompartment shells using building blocks from an organelle of unknown function. *J. Mol. Biol.* **426**, 2217–2228 (2014).
24. Dryden, K. A., Crowley, C. S., Tanaka, S., Yeates, T. O. & Yeager, M. Two-dimensional crystals of carboxysome shell proteins recapitulate the hexagonal packing of three-dimensional crystals. *Protein Sci.* **18**, 2629–2635 (2009).
25. Sutter, M. *et al.* Visualization of bacterial microcompartment facet assembly using high-speed atomic force microscopy. *Nano Lett.* **16**, 1590–1595 (2016).
26. Rodriguez-Ramos, J., Faulkner, M. & Liu, L. N. Nanoscale visualization of bacterial microcompartments using atomic force microscopy. *Methods Mol. Biol.* **1814**, 373–383 (2018).
27. Tanaka, S., Sawaya, M. R., Phillips, M. & Yeates, T. O. Insights from multiple structures of the shell proteins from the beta-carboxysome. *Protein Sci.* **18**, 108–120 (2009).
28. Cai, F., Sutter, M., Bernstein, S. L., Kinney, J. N. & Kerfeld, C. A. Engineering bacterial microcompartment shells: chimeric shell proteins and chimeric carboxysome shells. *ACS Synth. Biol.* **4**, 444–453 (2015).
29. Xue, B. *et al.* Structural disorder in viral proteins. *Chem. Rev.* **114**, 6880–6911 (2014).
30. Agirrezabala, X. *et al.* The near-atomic cryoEM structure of a flexible filamentous plant virus shows homology of its coat protein with nucleoproteins of animal viruses. *Elife* **4**, e11795 (2015).
31. Kinney, J. N., Axen, S. D. & Kerfeld, C. A. Comparative analysis of carboxysome shell proteins. *Photosynth. Res.* **109**, 21–32 (2011).
32. Park, J., Chun, S., Bobik, T. A., Houk, K. N. & Yeates, T. O. Molecular dynamics simulations of selective metabolite transport across the propanediol bacterial microcompartment shell. *J. Phys. Chem. B* **121**, 8149–8154 (2017).
33. Chowdhury, C. *et al.* Selective molecular transport through the protein shell of a bacterial microcompartment organelle. *Proc. Natl. Acad. Sci. U. S. A.* **112**, 2990–2995 (2015).
34. Sutter, M., Greber, B., Aussignargues, C. & Kerfeld, C. A. Assembly principles and structure of a 6.5-MDa bacterial microcompartment shell. *Science* **356**, 1293–1297 (2017).
35. Uddin, I., Frank, S., Warren, M. J. & Pickersgill, R. W. A generic self-assembly process in microcompartments and synthetic protein nanotubes. *Small* **14**, e1704020 (2018).
36. Mahinthichaichan, P., Morris, D. M., Wang, Y., Jensen, G. J. & Tajkhorshid, E. Selective permeability of carboxysome shell pores to anionic molecules. *J. Phys. Chem. B* **122**, 9110–9118 (2018).
37. Smart, O. S., Neduvelil, J. G., Wang, X., Wallace, B. A. & Sansom, M. S. HOLE: a program for the analysis of the pore dimensions of ion channel structural models. *J. Mol. Gr.* **14**, 354–360, 376 (1996).
38. Grosdidier, A., Zoete, V. & Michielin, O. SwissDock, a protein-small molecule docking web service based on EADock DSS. *Nucleic Acids Res.* **39**, W270–W277 (2011).
39. Friesner, R. A. *et al.* Extra precision glide: docking and scoring incorporating a model of hydrophobic enclosure for protein-ligand complexes. *J Med Chem* **49**, 6177–6196 (2006).
40. Long, B. M., Price, G. D. & Badger, M. R. Proteomic assessment of an established technique for carboxysome enrichment from *Synechococcus* PCC7942. *Can. J. Bot.* **83**, 746–757 (2005).
41. Dou, Z. *et al.* CO_2 fixation kinetics of *Halothiobacillus neapolitanus* mutant carboxysomes lacking carbonic anhydrase suggest the shell acts as a diffusional barrier for CO_2. *J. Biol. Chem.* **283**, 10377–10384 (2008).
42. Menon, B. B., Heinhorst, S., Shively, J. M. & Cannon, G. C. The carboxysome shell is permeable to protons. *J. Bacteriol.* **192**, 5881–5886 (2010).
43. Ritchie, R. J. Membrane potential and pH control in the cyanobacterium *Synechococcus* R-2 (*Anacystis nidulans*) PCC 7942. *J. Plant Physiol.* **137**, 409–418 (1991).
44. Barroso da Silva, F. L. & Dias, L. G. Development of constant-pH simulation methods in implicit solvent and applications in biomolecular systems. *Biophys. Rev.* **9**, 699–728 (2017).
45. Radak, B. K. *et al.* Constant-pH molecular dynamics simulations for large biomolecular systems. *J. Chem. Theory Comput.* **13**, 5933–5944 (2017).
46. Cai, F. *et al.* The pentameric vertex proteins are necessary for the icosahedral carboxysome shell to function as a CO_2 leakage barrier. *PLoS ONE* **4**, e7521 (2009).
47. Price, G. D., Badger, M. R., Woodger, F. J. & Long, B. M. Advances in understanding the cyanobacterial CO_2-concentrating-mechanism (CCM): functional components, Ci transporters, diversity, genetic regulation and prospects for engineering into plants. *J. Exp. Bot.* **59**, 1441–1461 (2008).
48. Larsson, A. M., Hasse, D., Valegard, K. & Andersson, I. Crystal structures of β-carboxysome shell protein CcmP: ligand binding correlates with the closed or open central pore. *J. Exp. Bot.* **68**, 3857–3867 (2017).
49. Cai, F. *et al.* The structure of CcmP, a tandem bacterial microcompartment domain protein from the beta-carboxysome, forms a subcompartment within a microcompartment. *J. Biol. Chem.* **288**, 16055–16063 (2013).
50. Faulkner, M., Zhao, L. S., Barrett, S. & Liu, L. N. Self-assembly stability and variability of bacterial microcompartment shell proteins in response to the environmental change. *Nanoscale Res. Lett.* **14**, 54 (2019).
51. Klein, M. G. *et al.* Identification and structural analysis of a novel carboxysome shell protein with implications for metabolite transport. *J. Mol. Biol.* **392**, 319–333 (2009).
52. Tanaka, S., Sawaya, M. R. & Yeates, T. O. Structure and mechanisms of a protein-based organelle in *Escherichia coli*. *Science* **327**, 81–84 (2010).
53. Rippka, R., Deruelles, J., Waterbury, J. B., Herdman, M. & Stanier, R. Y. Generic assignments, strain histories and properties of pure cultures of cyanobacteria. *J. Gen. Microbiol.* **111**, 1–61 (1979).
54. Thiel, T., Bramble, J. & Rogers, S. Optimum conditions for growth of cyanobacteria on solid media. *FEMS Microbiol. Lett.* **52**, 27–31 (1989).
55. Gust, B., Kieser, T. & Chater, K. F. *REDIRECT Technology: PCR-Targeting System in Streptomyces Coelicolor* (John Innes Centre, Norwich, 2002).
56. Casella, S. *et al.* Dissecting the native architecture and dynamics of cyanobacterial photosynthetic machinery. *Mol. Plant* **10**, 1434–1448 (2017).

57. Liu, L. N. *et al.* Control of electron transport routes through redox-regulated redistribution of respiratory complexes. *Proc. Natl. Acad. Sci. U. S. A.* **109**, 11431–11436 (2012).
58. Huang, F. *et al.* Roles of RbcX in carboxysome biosynthesis in the cyanobacterium *Synechococcus elongatus* PCC7942. *Plant Physiol.* **179**, 184–194 (2019).
59. Sun, Y. *et al.* Light modulates the biosynthesis and organization of cyanobacterial carbon fixation machinery through photosynthetic electron flow. *Plant Physiol.* **171**, 530–541 (2016).
60. Emsley, P. & Cowtan, K. Coot: model-building tools for molecular graphics. *Acta Crystallogr. D Biol. Crystallogr.* **60**, 2126–2132 (2004).
61. Emsley, P., Lohkamp, B., Scott, W. G. & Cowtan, K. Features and development of Coot. *Acta Crystallogr. D Biol. Crystallogr.* **66**, 486–501 (2010).
62. Phillips, J. C. *et al.* Scalable molecular dynamics with NAMD. *J. Comput. Chem.* **26**, 1781–1802 (2005).
63. Huang, J. & MacKerell, A. D. Jr. CHARMM36 all-atom additive protein force field: validation based on comparison to NMR data. *J. Comput. Chem.* **34**, 2135–2145 (2013).
64. Jo, S., Kim, T., Iyer, V. G. & Im, W. CHARMM-GUI: a web-based graphical user interface for CHARMM. *J. Comput. Chem.* **29**, 1859–1865 (2008).
65. Andersen, H. C. Rattle: A "velocity" version of the shake algorithm for molecular dynamics calculations. *J. Comput. Phys.* **52**, 24–34 (1983).
66. Darden, T., York, D. & Pedersen, L. Particle mesh Ewald: An N·log(N) method for Ewald sums in large systems. *J. Chem. Phys.* **98**, 10089–10092 (1993).
67. Kumar, S., Rosenberg, J. M., Bouzida, D., Swendsen, R. H. & Kollman, P. A. The weighted histogram analysis method for free-energy calculations on biomolecules. I. The method. *J. Comput. Chem.* **13**, 1011–1021 (1992).
68. Rosta, E. & Hummer, G. Free energies from dynamic weighted histogram analysis using unbiased Markov state model. *J. Chem. Theory Comput.* **11**, 276–285 (2015).
69. Berendsen, H. J. C., van der Spoel, D. & van Drunen, R. GROMACS: a message-passing parallel molecular dynamics implementation. *Comput. Phys. Commun.* **91**, 43–56 (1995).
70. Grosdidier, A., Zoete, V. & Michielin, O. EADock: docking of small molecules into protein active sites with a multiobjective evolutionary optimization. *Proteins* **67**, 1010–1025 (2007).
71. Roe, D. R. & Cheatham, T. E. 3rd. PTRAJ and CPPTRAJ: Software for processing and analysis of molecular dynamics trajectory data. *J. Chem. Theory Comput.* **9**, 3084–3095 (2013).
72. Case, D. A. *et al. AMBER 2017* (2017).

Acknowledgements

We thank Dr. Fang Huang and Dr. Yaqi Sun for the technical assistance in generating knockout mutants. This work was supported by Royal Society (UF120411, URF\R\180030, RGF\EA\181061, RGF\EA\180233, and RG130442 to L.-N.L.), the Biotechnology and Biological Sciences Research Council Grant (BB/M024202/1 and BB/R003890/1 to L.-N.L.), the Engineering and Physical Sciences Research Council (EP/N020669/1 and EP/R013012/1 to E.R.), and the funding from A*STAR Graduate Academy (A*GA) Singapore.

Author contributions

P.J.B., E.R., and L.-N.L conceived the project; M.F., I.S., S.L.W., F.S., and R.G.H. performed the simulations; M.F., I.S., S.L.W., F.S., and R.G.H. analyzed the data with input from P.J.B., E.R., L.-N.L.; M.F conducted the experimental studies and made the point mutations. M.F., S.L.W., E.R., and L.-N.L. wrote the paper with input from all authors.

Competing interests

The authors declare no competing interests.

Additional information

Supplementary information is available for this paper at https://doi.org/10.1038/s41598-020-74536-5.

Correspondence and requests for materials should be addressed to E.R. or L.-N.L.

Reprints and permissions information is available at www.nature.com/reprints.

Publisher's note Springer Nature remains neutral with regard to jurisdictional claims in published maps and institutional affiliations.

Supplementary Information

for

Molecular simulations unravel the molecular principles that mediate selective permeability of carboxysome shell protein

Matthew Faulkner[1#], István Szabó[2#], Samantha L. Weetman[1,3#], Francois Sicard[2], Roland G. Huber[3], Peter J. Bond[3], Edina Rosta[2*] & Lu-Ning Liu[1,4*]

[1] Institute of Integrative Biology, University of Liverpool, Crown Street, Liverpool L69 7ZB, United Kingdom

[2] Department of Chemistry, King's College London, London SE1 1DB, United Kingdom

[3] Bioinformatics Institute, Agency for Science, Technology and Research (A*STAR), Matrix 138671, Singapore, Singapore

[4] College of Marine Life Sciences, and Frontiers Science Center for Deep Ocean Multispheres and Earth System, Ocean University of China, Qingdao 266003, China

[#] These authors contributed equally to this work.

* Correspondence: edina.rosta@kcl.ac.uk (E.R.); luning.liu@liverpool.ac.uk (L.-N.L.)

Supplementary Table 1. Carbon fixation activities of Syn7942 strains tested in this study.

Strain	*Vmax* (μmol•min^{-1}•OD^{-1})	*Km*(RuBP) (mM)
WT	28.3 ± 2.0	0.7 ± 0.4
Δ*ccmK3*	17.4 ± 2.6	2.3 ± 0.7
Δ*ccmK4*	18.6 ± 1.6	2.3 ± 0.4
Δ*ccmP*	19.3 ± 11.1	7.7 ± 6.2
Δ*ccmK3K4*	3.6 ± 0.2	0.5 ± 0.1
ΔccmK2-S39A	9.9 ± 1.5	1.7 ± 0.6
Δ*ccmK3*+CcmK2-S39A	8.9 ± 1.6	1.4 ± 0.7
Δ*ccmK4*+CcmK2-S39A	4.8 ± 0.3	0.3 ± 0.1
Δ*ccmP*+CcmK2-S39A	2.9 ± 0.2	0.3 ± 0.1
Δ*ccmK3K4*+CcmK2-S39A	2.5 ± 0.4	0.7 ± 0.4

Supplementary Table 2. Wilcoxon rank-sum test *P* values for metabolite-protein contacts. The n value corresponds to the number of frames, when the substrate is either not within the contact cutoff of the residue, or when one or more atoms of the substrate is within the contact cutoff of the residue.

Substrate	Residue	*n* value		*P*-value (Wilcoxon rank-sum test)
		no contact	contact	
O_2	Arg11	2057	3	0.568
	Lly36	2038	22	0.122
	Ser39	2035	25	0.240
CO_2	Arg11	1185	5	0.890
	Lys36	1184	6	0.277
	Ser39	1167	23	0.086
HCO_3^-	Arg11	1958	422	0.698
	Lys36	2111	269	0.0002
	Ser39	1766	614	0.290
3-PGA	Arg11	1344	996	$3.797e^{-13}$
	Lys36	1856	484	0.013
	Ser39	1241	1099	$1.359e^{-17}$

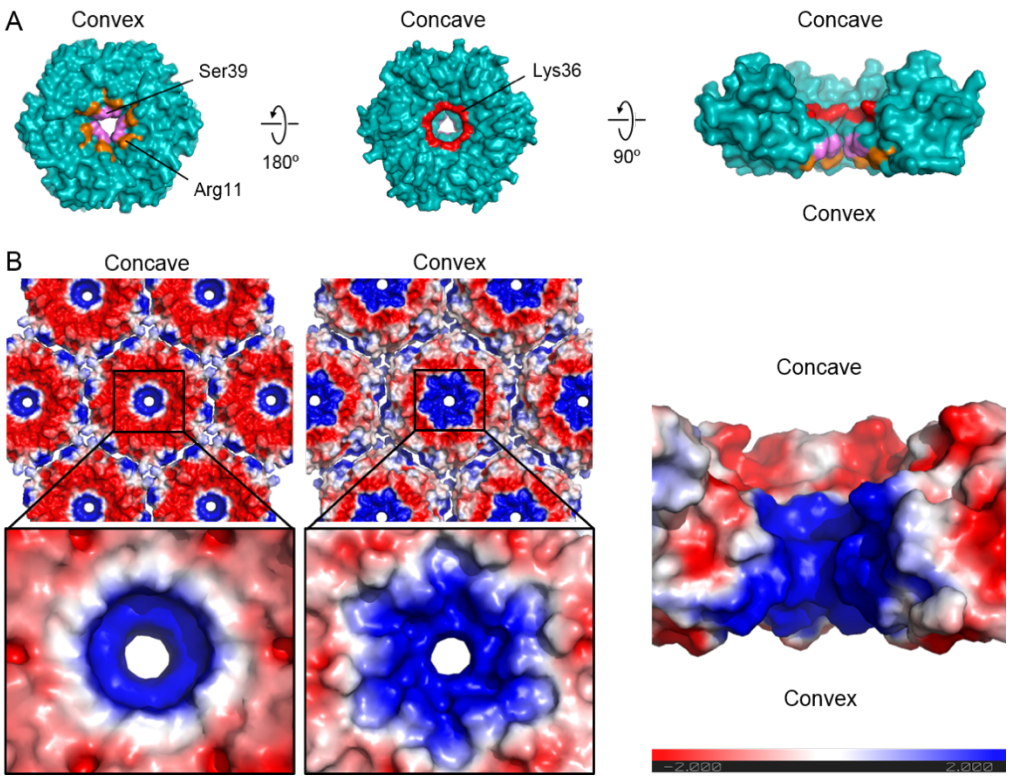

Supplementary Fig. 1. Structural analysis of CcmK2. A, Surface representations of CcmK2 (PDB: 3CIM) from different orientations, with Ser39, Lys36 and Arg11 residues highlighted in pink, red and orange, respectively. B, Electrostatic potential of CcmK2 (PDB: 2A1B), with the negatively charged residues in red and positively charged residues in blue. The concave side of CcmK2 is mostly negatively charged and a large area of the convex side has positive electrostatic potential, indicative of the charged-based tuning mechanism of the pore for molecular passage. The central pore is positively charged, due to the positively charged residues Lys36 and Arg11. The electrostatic potential was calculated using PyMOL with APBS plugin.

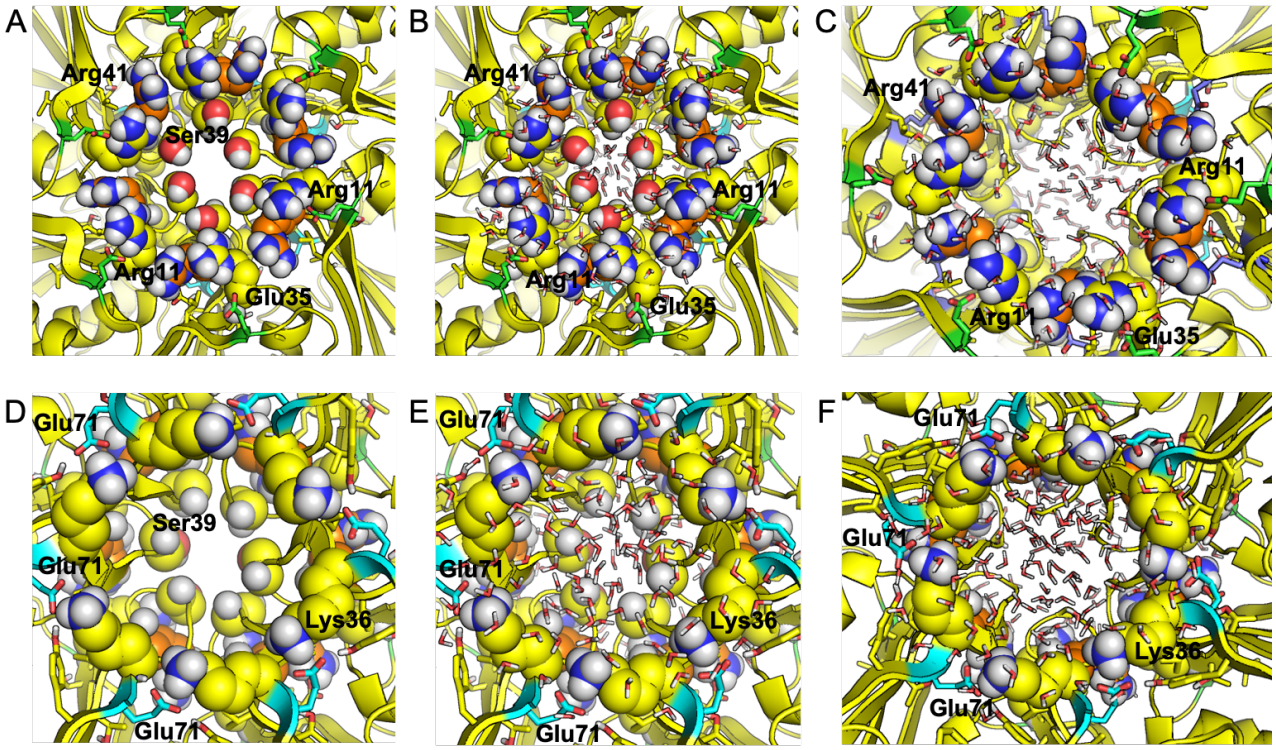

Supplementary Fig. 2. Convex (A-C) and concave (D-F) sides of the pore. Key positively charged Arg (A-C, yellow and orange VDW spheres) and Lys (D-F, yellow VDW spheres) residues are lined up at the pore entrance, directly stabilized by salt bridges via key Glu residues (green and blue sticks respectively) as well as solvent water molecules. Ser39 forms the bottleneck of the pore (A-B, D-E, yellow and red VDW spheres). Furthermore, water molecules also occupy the middle of the pore (B-C, E-F, sticks). Note that the convex side is lined up by two sets of positively charged residues (Arg11 and Arg41) occluding the pore entrance more than the concave side with Lys36 presenting a less charged environment and a larger diameter.

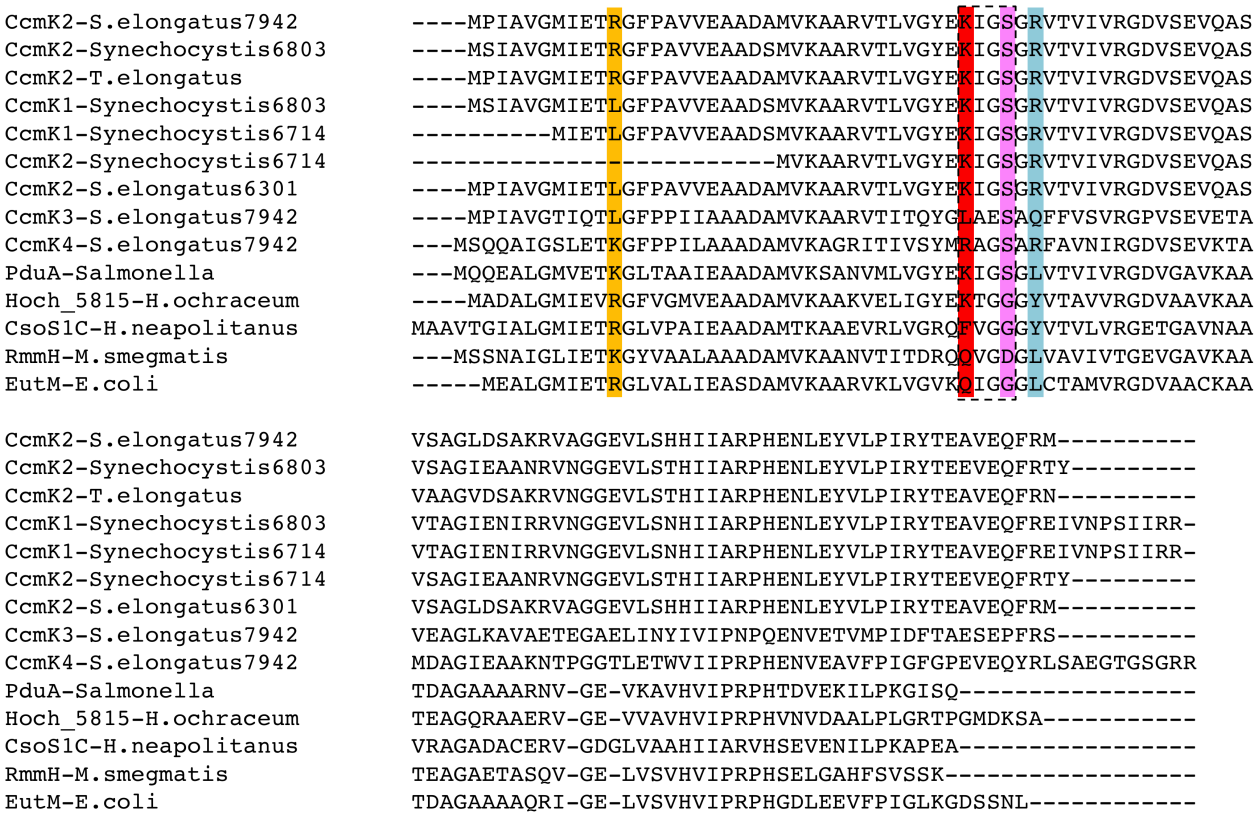

Supplementary Fig. 3. Protein sequence alignment of BMC shell hexamer homologs. The three key residues of interest Ser39, Lys36, and Arg11 are highlighted in pink, red, and orange, respectively. Ser39 and Lys36 in the pore motif of K-I-G-S are conserved among shell protein homologs. Arg11 is located at the pore entrance on the convex side of CcmK2 along with Arg41 that is highlighted in aqua.

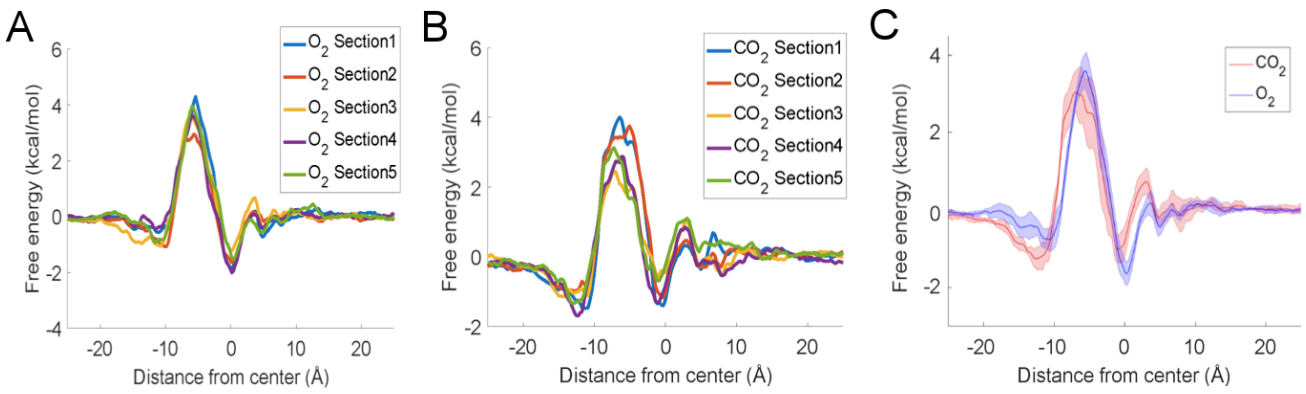

Supplementary Fig. 4. Free energy profile reconstruction. To assess the convergence of the US simulations in the reconstruction of the representative free energy profiles, we divided each US simulation window into 5 equal-length trajectories (sections) and analyzed them independently, as shown for the O_2 molecule (A) and the CO_2 molecule (B). We checked the independent profiles did not display significant systematic changes and calculated the mean and standard error for the representative 1D(z) free energy profiles (C).

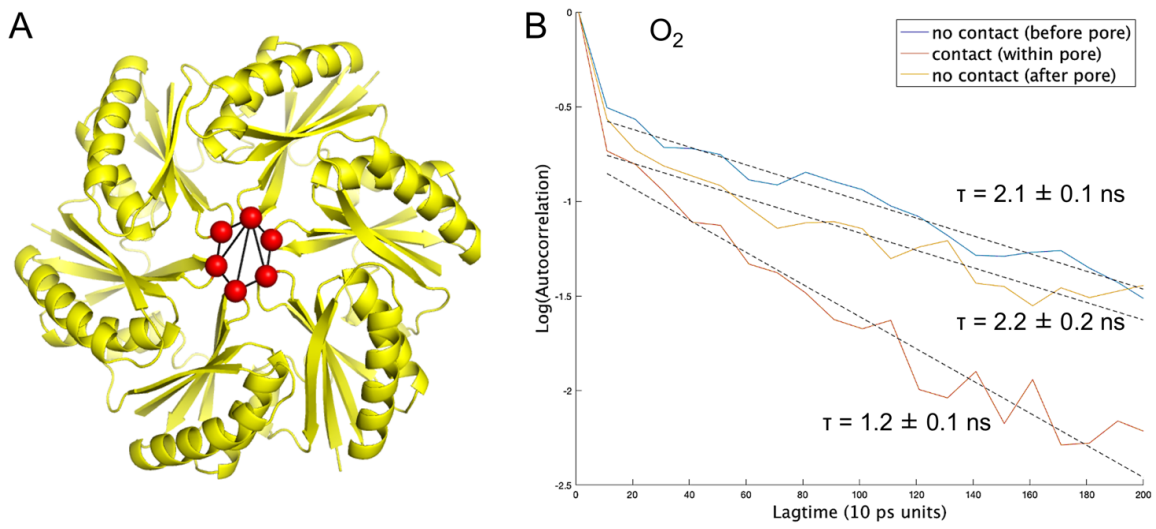

Supplementary Fig. 5. Delaunay triangulation of the pore and autocorrelation. A, Triangulated hexagon defined via the Ser39 CA atoms of the 6 loops (red points) defining the pore entrance that lie approximately on a plane, used to estimate the 2D surface area of the pore. B, The autocorrelation time, τ, associated with the temporal evolution of the pore surface area of CcmK2 from the Umbrella Sampling trajectories for O_2. We considered 3 representative US windows along the Z axis when the metabolite is located at Z = -20 Å (blue, convex side), Z=-5 Å (red, within the pore region), and Z = 20 Å (yellow, concave side). We expect that no large conformational changes take place orthogonal to our collective variable. As the pocket size is relatively large, the US windows are long enough to enable the smaller conformational changes during our MD simulations either driven by the US reaction coordinate, or, if orthogonal to this, during the MD simulations in each window. Nevertheless, we cannot exclude that at even longer timescales further conformational changes may occur at the pore, especially taking into account other components of the system (e.g., C-terminus, or other proteins interacting with the shell) not included in our simulations.

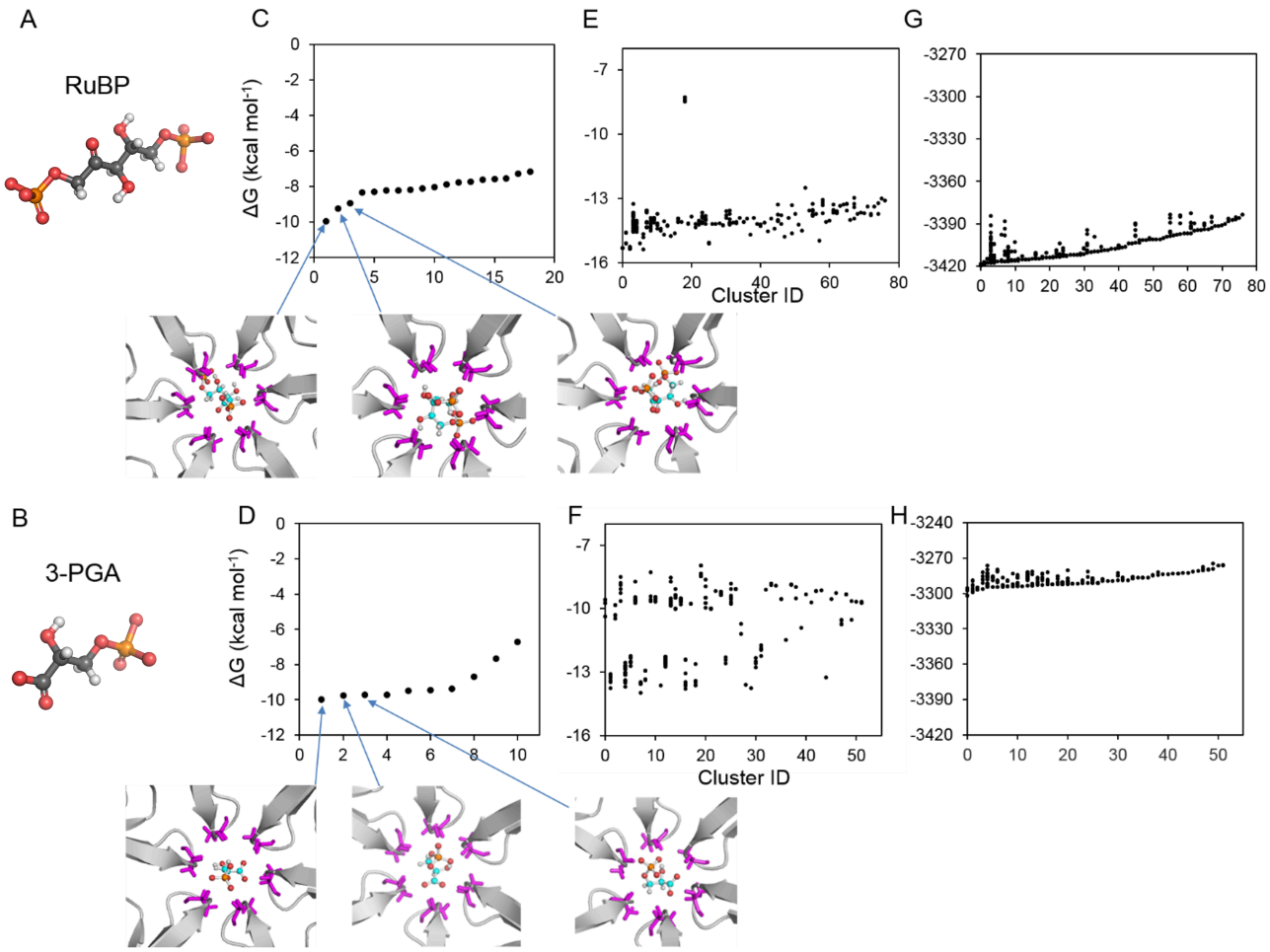

Supplementary Fig. 6. Molecular docking of RuBP and 3-PGA with CcmK2 using SwissDock and Glide SP. A-B, Ball-and-stick representation of the most likely protonation state of RuBP and 3-PGA molecules at ~pH7. See Fig. 6A. C-D, Free energy profiles of RuBP and 3-PGA docking to CcmK2 using Glide XP, the three lowest free energy poses are shown underneath, and the corresponding data points are indicated by blue arrows. E-F, Free energy profiles of RuBP and 3-PGA docking to CcmK2 using SwissDock. G-H, FullFitness plots of RuBP and 3-PGA using SwissDock.

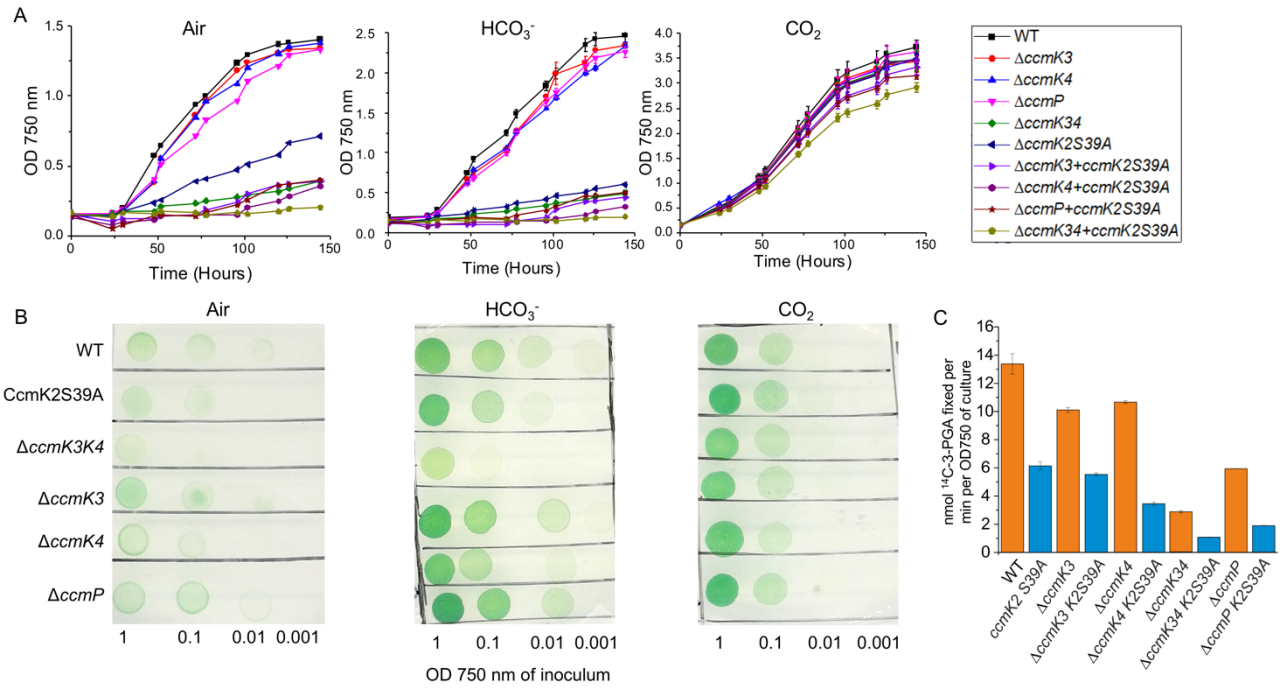

Supplementary Fig. 7. Physiology of strains in air, HCO_3^- and CO_2 conditions. A, Growth curves of strains in air, HCO_3^- and 4% CO_2 conditions, respectively (*n* = 3). B, Spot assays of the strains grown on BG11 plates in air, HCO_3^- and 4% CO_2 conditions (*n* = 2) after 48 hours. C, Rubisco activities of cells grown under 4% CO_2, measured by ^{14}C radiometric carbon fixation assay at 0.4 mM RuBP (*n* = 3).